Avalanche criticality in individuals is associated with fluid intelligence and working memory capacity

Longzhou Xu[1], Lianchun Yu[1,2], Jianfeng Feng[3,4]

[1]School of Physical Science and Technology, and Key Laboratory for Magnetism and Magnetic Materials of MOE, Lanzhou University, Lanzhou, 730000, China

[2]The School of Nationalities' Educators, Qinghai Normal University, Xining, 810000, China

[3]Institute of Science and Technology for Brain Inspired Intelligence, Fudan University, Shanghai, 200433, China

[4]Department of Computer Science, University of Warwick, Coventry, CV4 7AL, UK

These authors contributed equally: Longzhou Xu, Lianchun Yu
Corresponding authors: Correspondence to Lianchun Yu, or Jianfeng Feng

Abstract

The critical brain theory suggests that efficient neural computation could be realized by critical brain dynamics hallmarked by scale-free avalanche activity. However, further verification and application of this theory requires not only accurately identifying the critical point but also depicting the phase transition in brains so that different cognitive states could be mapped on a spectrum. In this work, we mapped individuals' brains onto an inverted-U curve between the mean synchronization and synchronization entropy of blood oxygenation level-dependent (BOLD) signals from resting-state fMRI scans. We found that the critical point lies at the tipping point (i.e., moderate synchrony and maximal variability in synchrony) of this curve. We then verified that the complexity of functional connectivity, as well as the coupling between structural and functional networks, was maximized near the critical point, whereas reduction in complexity and structure-function decoupling were found both in the sub- and supercritical regimes. We then observed order-disorder phase transitions in resting-state brain dynamics and found that the brains showed longer dwell times in the subcritical regime. These results provided strong evidence that the large-scale brain networks were hovering around the critical point. Finally, we found that critical dynamics were associated with high scores in fluid intelligence and working memory tests but not crystallized intelligence scores. We identified brain regions whose critical dynamics showed significant positive correlation with fluid intelligence performance, and found these regions were located in prefrontal cortex and inferior parietal cortex, which were believed to be important nodes of brain networks underlying human intelligence. Our results revealed the role that avalanche criticality plays in cognitive performance, and provide a simple method to identify the critical point and map cortical states on a spectrum of neural dynamics, with a critical point in the domain.

Introduction

The critical brain hypothesis posits that the brain perches in close vicinity to a critical point between order and disorder, hallmarked by power-law scaling of event size distributions[1,2]. This hypothesis is supported by the breadth of observations of power-law scaling in many different systems using various approaches[3-9]. At the same time, the argument has also been strengthened by advantages in information transmission, information storage, and nonlinear input filters for neural systems operating near criticality[10-12], evidenced by both theoretical and experimental work[13]. Meanwhile, this hypothesis still faces challenges from several perspectives[14]. For example, power laws could emerge from simple stochastic processes or noncritical neuronal systems, so power laws alone are not convincing evidence for criticality[15]. As it has been asked, "If the brain is critical, what is the phase transition?[16]" Indeed, the observation of power law avalanche activity along with phase transition between order and disorder would be more persuasive for criticality. Furthermore, though previous studies have associated supercriticality with reduced consciousness[9,17], near-critical dynamics with rest[18], and subcriticality with focused cognitive states[19], there remains a gap between the specific brain state and efficient information processing endowed by criticality as predicted by theory[20]. To fully understand the functional roles of critical and non-critical dynamics, more research is required to relate brain states and cognitive performance to neural dynamics that lie on a spectrum, ranging from subcriticality to supercriticality. Therefore, it is vital to develop data analysis methods to depict this phase spectrum with high resolution and characterize the subsequent reorganization of brains with the transition in this spectrum[16].

With advances in brain imaging techniques such as functional magnetic resonance imaging (fMRI), the critical brain theory has found roles in interpreting fundamental properties of large-scale brain networks in the context of structure-dynamics-function relationships[21,22]. For example, it has been shown that the structural connections of brains are mostly reflected in the functional networks as the brain dynamics are at the

critical point, and this structure-function coupling is disrupted when brains are moving away from criticality during anesthesia[23]. Another application of criticality is to explain the dynamic basis of brain complexity[24-26]. In particular, functional connectivity (FC) complexity, which is an umbrella term describing the variability, diversity, or flexibility of functional connections in brain networks, has been associated with cognitive performance from many perspectives, such as high-order cognition, aging, and cognitive impairment in brain disorders[27-31]. Studies have suggested that the FC complexity is possibly at its maximum at the critical point, while its capacity is provided by special topological properties of the structural network, such as hierarchical modular organization[32,33].

To validate these applications, both computer modeling methods and experimental data analysis methods were used. Computer modeling utilizes structural imaging data to model large-scale brain dynamics and then functional networks[34,35]. However, there is still disagreement on which type of phase transition should be adopted for large-scale brain networks, e.g., first-order discontinuous vs. second-order continuous phase transitions and edge of chaos criticality vs. avalanche criticality[36,37]. Experimental studies usually take advantage of dynamic changes caused by interventions, such as deprived sleep, anesthesia, or brain diseases, to show deviations from criticality and subsequent reorganization of FC networks[9,23,38,39]. However, deviations caused by these interventions are usually unidirectional, either in the sub- or supercritical directions. Furthermore, it is not clear whether deviations from criticality caused by different intervention methods follow an identical phase transition trajectory. Recent studies have proposed the concept of a “critical line” instead of a “critical point” and suggested that multiple phase transition trajectories may exist[40]. Therefore, the successful recovery of the phase transition trajectory from a large-scale brain network will not only help to answer key questions regarding what the phase transition is if the brain is critical but also have important implications in brain functional imaging and large-scale brain modeling.

In this study, we used the inverted-U trajectory for mean synchronization (MS) vs.

synchronization entropy (SE) of blood oxygenation level-dependent (BOLD) signals from resting-state fMRI (rfMRI) scanning to identify the critical point and phase transition in large-scale brain networks. This inverted-U trajectory for MS vs. SE was first reported by Yang et al.[12] They predicted that moderate mean and high variability in synchrony would emerge at the critical point with balanced excitation-inhibition (E-I) in the computer model, and demonstrated this fact in rat cortex slice culture with drug-induced E-I imbalance and loss of criticality. Later, Meisel et al. used EEG recordings to find increased MS with decreased SE as brains shift from the critical point toward a supercritical regime during prolonged wakefulness[9]. These studies presaged that the moderate mean and maximal variability in synchrony could be a signature for criticality that exists at different levels of neural systems. We took individual subjects' brain resting state characterized by MS and SE as a representation of the state (averaged in scan duration) that the brain system could be ergodic. We portrayed each subject's brain state as a point in the MS vs. SE phase plane. These points formed an inverted-U phase trajectory, which we believe reflected order -disorder phase transition in large-scale brain networks.

We then used the avalanche distribution analysis method to confirm that the tipping point of this inverted-U curve was nearest to the critical point, which separates the ordered/supercritical and disordered/subcritical regimes. Based on the above discovery, we further examined previous conjectures on criticality in large-scale brain networks and found that both FC complexity and structure-function coupling were maximized around the critical point. We utilized the sliding window approach to demonstrate the instantaneous phase transition that occurred in individual brains. We showed that brains lingering in the subcritical regime exhibited longer dwell time than those in other regimes. Finally, we found that subjects whose brains were closer to the critical point yielded high scores in fluid intelligence and working memory tests. What's more, the critical dynamics in prefrontal cortex and supramarginal gyrus, which were believed as vital regions in the networks of Parieto-Frontal Integration Theory (P-FIT) for intelligence[41], showed significant correlations with fluid

intelligence performance.

Materials and Methods

fMRI data acquisition and preprocessing

We used resting-state fMRI (rfMRI) data from the Human Connectome Project (HCP) 1200-subject release[42]. Each subject underwent two sessions of rfMRI on separate days, each session with two separate 14 min 24s acquisitions generating 1200 volumes on a customized Siemens 3T Skyra scanner ($\mathrm{TR} = 720\ \mathrm{ms}$, $\mathrm{TE} = 33\ \mathrm{ms}$, flip angle $= 52°$, voxel size $= 2$ mm isotropic, 72 slices, $\mathrm{FOV} = 208 \times 180\mathrm{mm}$, matrix $= 104 \times 90$ mm, multiband accelaration factor $= 8$, echo spacing $= 0.58$ ms). The rfMRI data used for our analysis were processed according to the HCP minimal preprocessing pipeline[43,44] with denoising procedures developed by the HCP that removed artifacts using FMRIB's ICA-based X-noisifier[45]. We used only the left-to-right acquisitions from the first resting-state dataset (i.e., resting state fMRI 1 FIX-denoised package).

The first 324 subjects in the dataset entered into our study, and we excluded 29 subjects for missing data. This left us with 295 subjects for further analysis, and 162 of them were females. All the participants were between the ages of 22-36, 58 were between the ages of 22-25, 130 were between the ages of 26-30, 104 were between the ages of 31-35, and 3 were 36 years old.

For global network analysis, the whole cortex was parcellated into 96 regions (https://identifiers.org/neurovault.image:1699), and from each region the time series averaged across the voxels were extracted and Z-normalized to construct region of interesting (ROI) signals for further analysis. For regional analysis, the whole brain was parcellated into 246 regions with Human Brainnetome Atlas, which contains 210 cortical and 36 subcortical subregions (http://atlas.brainnetome.org/bnatlas.html).

Then the voxel-wise signals were Z-normalized for further analysis.

Diffusion tensor imaging (DTI) data acquisition and preprocessing

The diffusion MRI images used in this study were also from the HCP 1200-subject release[46]. Briefly, the diffusion data were collected using a single-shot, single refocusing spin-echo, echo-planar imaging sequence (TR = 5520 ms, TE = 89.5 ms, flip angle = 78 °, FOV = 210 × 180 mm, matrix = 168 × 144 mm, voxel size = 1.25 mm istropic, slices = 111, multiband acceleration factor = 3, echo spacing = 0.78 ms). Three gradient tables of 90 diffusion-weighted directions and six b=0 images each, were collected with right-to-left and left-to-right phase encoding polarities for each of the three diffusion weightings (b=1000, 2000, and 3000 s/mm^2). All diffusion data were preprocessed with the HCP diffusion pipeline (updated with EDDY 5.0.10)[46], and the details are provided at https://www.humanconnectome.org. In this study, from the 295 selected subjects, only 284 subjects were entered into our DTI data analysis because 11 of them were missing the corresponding DTI data.

The structure connectivity matrix was constructed using DSI Studio (http://dsi-studio.labsolver.org). The diffusion data were reconstructed in the Montreal Neurological Institute (MNI) space using q-space diffeomorphic reconstruction[47] to obtain the spin distribution function[48]. A diffusion sampling length ratio of 1.25 was used. The restricted diffusion was quantified using restricted diffusion imaging[49], and a deterministic fiber tracking algorithm[50] was used to obtain one million fibers with whole-brain seeding. The angular threshold was randomly selected from 15 degrees to 90 degrees. The step size was randomly selected from 0.1 voxels to 3 voxels. The anisotropy threshold was automatically determined by DSI Studio. The fiber trajectories were smoothed by averaging the propagation direction with a percentage of the previous direction. The percentage was randomly selected from 0% to 95%. Tracks with a length shorter than 5 or longer than 300 mm were discarded. The same brain atlas from the resting-state fMRI data global analysis was used, and the

connectivity matrix was calculated by using the count of the connecting tracks.

Cognition measures

We examined associations between intelligence and critical dynamics conducted in our rfMRI analysis. Three relevant behavioral tasks were used as a measure of cognitive ability, including fluid intelligence, working memory, and crystallized intelligence. The same 295 subjects were also entered into our cognitive ability analysis, but for the fluid intelligence analysis, 4 subjects were excluded due to missing intelligence scores.

The fluid intelligence scores in the HCP data release were measured using the number of correct responses on form A of the Penn Matrix Reasoning Test (PMAT, $\text{mean} = 17.01$, $\text{standard deviation (SD)} = 4.91$, $\text{range} = 4 - 24$)[51,52], which had 24 items and 3 bonus items, using nonverbal visual geometric designs with pieces to assess reasoning abilities that can be administered in under 10 min. The PMAT[53] is an abbreviated version of Raven's Standard Progressive Matrices test (RSPM)[54], which comprises 60 items.

Crystallized intelligence was measured using the picture vocabulary test from the National Institutes of Health toolbox[51,52]. This measure of receptive vocabulary was administered in a computer-adaptive testing (CAT) format. The participant was presented with four pictures and heard an audio recording saying a word. The participant was instructed to select the picture that most closely showed the meaning of the word. Because the test used a variable length CAT with a maximum of twenty-five items, some participants had fewer items. The presented words depended on the participant's performance. Raw scores were converted to age-adjusted scores. Here, we included only the unadjusted scores (Picture vocabulary, mean=116.9, SD=10.16, range=92.39-153.09).

Working memory was assessed using the List Sorting Working Memory test from the NIH Toolbox[51], in which the participants were required to sequence sets of visually

and a small number of orally presented stimuli in size order from smallest to biggest. Pictures of different foods and animals were displayed with both a sound clip and a written test that names them, and involved two different conditions. In the 1-list condition, participants ordered a series of objects, either food or animals, but in the 2-list condition, participants were presented with both animal and food lists and asked to order each list by increasing size. The number of list items increased in subsequent trials, and the task was discontinued after 2 consecutive incorrect trials. Raw scores were the sum of the total correct items, which were converted to age-adjusted scores. Here, we included only the unadjusted scores (List sorting, mean=111.13, SD=12.02, range=84.83-144.50).

Synchrony and variability in synchrony

We measured the mean and variability in synchronization with a previously described approach[9,12]. First, we obtained the phase trace $\theta_j(t)$ from the *j-th* ROI signal $F_j(t)$ using its Hilbert transform $H[F_j(t)]$:

$$\theta_j(t) = arctan\frac{H[F_j(t)]}{F_j(t)}. \quad (1)$$

Next, we calculated the Kuramoto order parameter as follows:

$$r(t) = \frac{1}{u}\left|\sum_{j=1}^{u} e^{i\theta_j(t)}\right|, \quad (2)$$

in which $u = 96$ is the number of ROIs of the cerebral cortex. The Kuramoto order parameter $r(t)$ was used as a time-dependent measure of phase synchrony of the whole system. The MS in a time period was calculated as

$$\langle r \rangle = \frac{1}{V}\sum_{t=1}^{V} r(t), \quad (3)$$

where V is the length of the time period. In this study, we calculated static MS in the entire scan period with V=1200 time points and dynamic MS in a sliding window with V= 200 time points and a sliding step of 10 time points. We derived the entropy of $r(t)$ as the measure of variability in synchronization (SE):

$$H(r) = -\sum_{n=1}^{N} p_n \, log_2 \, p_n, \quad (4)$$

where p_n is the probability that $r(t)$ falls into a bin between $b_n < r(t) < b_{n+1}$. In this study, we chose the number of bins $N = 30$, and the robustness of our results was also tested with an interval between 5 and 100.

To verify that the calculated inverted-U curves between MS and SE were not due to noise but essentially reflected the dynamics of the fMRI data, we constructed randomized surrogate datasets with the phase randomization method[55]. The phase randomization procedures were as follows: (1) take the discrete Fourier transformations of normalized ROI signals of each subject; (2) rotate the phase at each frequency by an independent random variable that was uniformly chosen in the range $[0, 2\pi]$. Crucially, the different time series were rotated by the different phases at the same time point to randomize the phase information[56]; (3) then apply the inverse discrete Fourier transformation to these time series to yield randomized copies. We generated 500 phase-shuffling surrogate time series for each ROI of each subject and then calculated $\langle r \rangle$ and $\mathrm{H}(r)$ to obtain the relationship between $\langle r \rangle$ and $\mathrm{H}(r)$ from surrogate data.

Avalanche analysis

In our avalanche analysis, the normalized ROI signals were reduced to a spatiotemporal point process by detecting the suprathreshold peak positions intermediate between two above-threshold time points, as shown in the example of Fig. 1 **a**. By binning the binary sequences with appropriate time resolution (time bin), we obtained a spatial pattern of active ROIs within consecutive time bins. An avalanche was defined as a series of consecutively active bins, which were led and followed by blank bins without activations. The size S and duration T of the avalanches were then defined as the total number of activations and total number of time bins during this avalanche, respectively[6,8].

If a system operates near a critical point, the size distribution ($P(S)$), duration

distribution ($P(T)$), and average size for a given duration ($\langle S\rangle(T)$) should be fitted into power laws:

$$P(S) \sim T^{-\alpha}, \tag{5}$$

$$P(T) \sim T^{-\tau}, \tag{6}$$

$$\langle S\rangle(T) \sim T^{\gamma}, \tag{7}$$

where α, τ, and γ are critical exponents of the system[57,58]. Furthermore, the following relationship was proposed as an important evaluation of the critical system[16,57], namely,

$$\frac{\tau-1}{\alpha-1} = \gamma. \tag{8}$$

In this study, we defined

$$\delta = \left|\frac{\tau-1}{\alpha-1} - \gamma\right| \tag{9}$$

to measure the distances of the systems from the critical point, so the smaller δ is, the closer the systems are to the critical point. However, it is noted that Touboul and Destexhe claimed that Eqs. (5)-(8) can be obtained in systems that are not critical[59].

The scaling exponents governing the power-law distribution were estimated using the maximum likelihood estimator (MLE)[60,61]. Briefly, the MLE procedure supposed that the empirical data sample was from a power-law function in the range (x_{min}, x_{max}), with probability density $\frac{1}{\sum_{x=x_{min}}^{x_{max}} (\frac{1}{x})^{\alpha}} \left(\frac{1}{x}\right)^{\alpha}$ 16. In this study, the lower bound x_{min} was set to 3 (some cases set to 2 will be specified in the context) events for size distributions and 3 time bins for duration distributions, and the upper bound x_{max} was set to 30 events for size distributions and 9 time bins for duration distributions. Next, we estimated critical exponents α and τ by maximizing the likelihood function and via a lattice search algorithm[61]. We then used Clauset's goodness-of-fit test to quantify the plausibility of fits[60-62]. We used a power-law model to produce data sets over the fit range and compared the Kolmogorov–Smirnov (KS) statistics between (1) the real data and the fit against (2) the model data and the fit. If the real data produced

a KS-statistic that was less than the KS-statistic found for at least 20% of the power-law models (i.e., $p \geq \mathrm{p}_{thresh} = 0.2$)[61], we accepted the data as being fit by the truncated power law because the fluctuations of the real data from the power law were similar in the KS sense to random fluctuation in a perfect power-law model.

Branching parameter

The branching parameter σ, which is defined as the average number of subsequent events that a single preceding event in an avalanche triggers, is a convenient measure to identify criticality[8]. In theory, the system is critical for $\sigma = 1$ and sub- (super) critical for $\sigma < 1 (\sigma > 1)$. In this study, σ was calculated as

$$\sigma = \frac{1}{N} \sum_{i=1}^{N} \frac{n_i^*}{n_i}, \tag{10}$$

where n_i is the number of ancestors, n_i^* is the number of descendants in the next time bin, and N is the total number of time bins with activations.

Definition of kappa

A nonparametric measure, κ, for neuronal avalanches was introduced by Shew and his colleagues[11]. It quantifies the difference between an experimental cumulative density function (CDF) of the avalanche size, $\mathrm{F}(\beta_k)$, and the theoretical reference CDF, $F^{NA}(\beta_k)$, which is a power-law function with theoretical expected exponent $\alpha = 1.5$:

$$\kappa = 1 + \frac{1}{m} \sum_{k=1}^{m} (F^{NA}(\beta_k) - F(\beta_k)), \tag{11}$$

where β_k are avalanche sizes logarithmically spaced between the minimum and maximum observed avalanche sizes, and m is the number of histogram bins. The unit value of κ is characteristic of the system in a critical state, whereas values below and above 1 suggest sub- and supercritical states, respectively.

Functional connectivity matrix

We constructed an FC matrix by computing the Pearson correlation C_{ij} between ROI i and ROI j, and the mean FC strength $\langle FC \rangle$ was obtained by

$$\langle FC \rangle = \langle |C_{ij}| \rangle, \tag{12}$$

where $|\cdot|$ means the absolute value.

Functional connectivity entropy

The FC entropy, $H(FC)$, used in this study was similar to the early work of Yao et al[63], which is calculated by

$$H(FC) = \sum_i - p_i log_2(p_i), \tag{13}$$

where p_i is the probability distribution of $|C_{ij}|$, i.e., $\sum_i p_i = 1$. In the calculation, the probability distribution was obtained by discretizing the interval (0, 1) into 30 bins.

Functional connectivity diversity

As defined in the recent work of Wang et al[32], the functional diversity ($D(FC)$) of the FC network is measured by the similarity of the distribution to the uniform distribution:

$$D(FC) = 1 - \frac{1}{N_M} \sum_{i=1}^{M} \left| p_i - \frac{1}{M} \right|, \tag{14}$$

where $N_M = 2\frac{M-1}{M}$ is a normalization factor, $D(FC)$ is in the range [0, 1], and p_i is the probability distribution of $|C_{ij}|$, which was obtained by discretizing the interval (0, 1) into M bins (M=30 in this work). For completely asynchronous or synchronized states, the correlation values fall in one bin at 0 or 1, where $D(FC) = 0$ reflects the simple dynamic interaction pattern. In an extreme case where all types of FC

equivalently exist, p_i would ideally follow a uniform distribution (i.e., probability in each bin $= \frac{1}{M}$) and $D(FC) = 1$.

Functional connectivity flexibility

To measure the flexibility of FC among different brain regions, we used the sliding window approach to calculate connectivity number entropy (CNE) for each region[33]. For the 96 ROIs, a non-overlapping sliding window method was applied to the 96 ROI signals extracted from these regions. The choice of window size must be sufficient to yield a stable Pearson's correlation coefficient within each window, yet small enough to reveal the temporal-dependent variation in FC. We chose a window size in the range of 20-30, corresponding to the number of windows (n_{win}) in the range of 40-60.

With each time window, we first calculated the correlation matrix of 96 brain regions with their time series in this window, and then, we obtained the brain network matrix by binarizing the correlation matrix of 96 brain regions with threshold THR_{FC}. Therefore, for a particular region k ($k = 1, 2,$ ... 96), we counted the number of regions connected to it in each time window. Then, over the whole scan time, we could obtain the distribution of all possible connection numbers observed for this region. From this distribution, we calculated p_i, the probability for a particular connection number occurring, where i indicated the $i\text{-}th$ connection number among all possible connection numbers. Subsequently, CNE for the region k is a complexity measure (i.e., Shannon entropy) for the disorder in the connection numbers over time:

$$CNE_k = -\sum_{i=1}^{95} p_i log_2 p_i, \tag{15}$$

where the summation index runs from 1 to the number of all possible connection numbers.

For each subject, the CNE at the whole-brain level was obtained by simply averaging the regional CNE_k values over 96 regions:

$$CNE = \frac{1}{96}\sum_{k=1}^{96} CNE_k. \quad (16)$$

Similarity between functional and structural networks

To measure the similarity between functional and structural connection networks, the FC matrices C_{ij} were thresholded by THR_{FC} to yield binary adjacency matrices A_{ij} such that $A_{ij} = 1$ if $C_{ij} \geq THR_{FC}$, and $A_{ij} = 0$ otherwise. The parameter THR_{FC} was chosen to fix link density ρ_{FC}, which was defined as the ratio of the connections in the network ($\sum_{i>j} A_{ij}$) to the total possible number of connections. It is important to fix the link density when comparing networks, as otherwise, differences could arise because the means of the respective C_{ij} are different (and therefore the number of nonzero entries in A_{ij}) but not because connections are topologically reorganized across conditions[23].

The constructed FC networks for each subject were compared with the group-aggregated structural connectivity (SC) network but not the individual's SC network to avoid fluctuations in individual SC networks due to errors in the DTI track. First, the binary adjacency matrices of structural connection B_{ij} were obtained for each subject such that $B_{ij} = 1$ if there were tracked fiber links; otherwise, $B_{ij} = 0$. Then, the binary adjacency structural connection matrices were summed up and again thresholded by a thresholding value THR_{SC} to yield a group-aggregated matrix B_g. In this way, high THR_{SC} values would exclude connections that were shared by fewer subjects but preserve connections that were common in most subjects.

To estimate the similarity between the FC network of each subject and the group-aggregated structural network B_g, we computed the Pearson correlation $R(FC - SC)$ and Hamming distance $HD(FC - SC)$ between these two networks[23]. Specifically, the Hamming distance is defined as the number of symbol substitutions

(in this case 0 or 1) needed to transform one sequence into another and vice versa, and in this case, it is equal to the number of connections that must be rewired to turn the functional network neighbor into the structural network neighbor.

Dynamic analysis of phase transitions

We used the sliding window approach to capture the time-dependent changes in measures used in this study. In the calculation, the length of the sliding window was set to $W = 200$ (volumes), and the sliding step was set to $\Delta n = 10$ (volumes). In each window, we calculated the corresponding dynamic measures, including dynamic MS $\langle r \rangle_n$, dynamic SE $H(r)_n$, and dynamic FC matrix $\left(C_{ij}\right)_n$. From the dynamic FC matrix $\left(C_{ij}\right)_n$, we further obtained dynamic FC entropy $H(FC)_n$, FC diversity $D(FC)_n$, Pearson correlation between FC and SC $R(FC - SC)_n$, and Hamming distance $HD(FC - SC)_n$.

Results

1 The signature of critical dynamics in the cortical network

For the 295 available subjects, we first investigated the power-law distribution of avalanche size at the population level. After preprocessing, the normalized ROI signals were converted into point processes in which each time point represented an activation. In previous studies, activations were usually defined as threshold-crossing events[6]. However, in this study, we defined the activation as the time point when the BOLD signals reached their peak value, while the signals one step before and after this time point were above the chosen threshold (Fig. 1 **a**). We then calculated the avalanche size distribution $P(S) \sim S^{-\alpha}$ (Fig. 1 **b**), as well as the avalanche duration distribution $P(T) \sim T^{-\tau}$ (Fig. 1 **c**). First, from the estimated α and τ values, we tested whether the relationship between the scaling exponent holds for different thresholds

of ROI signals[16,57]. We found that the closest matching occurred when the chosen threshold was around 1.4 SD (Fig. 1. **d**). Second, the power-law distribution of avalanche size with a slope of $\alpha = 1.5$ could be predicted by theory for a critical branching process with branching parameter $\sigma = 1$ [64,65]. However, we found that the threshold of 1.4 SD yielded $\sigma = 0.91$ and $\alpha = 1.56$ (Fig. 1 **d**), which did not match well with the theoretical prediction.

As the above close check of hallmarks of criticality did not agree with each other well, we moved forward to investigate whether this mismatch could be a result of intersubject variability. We calculated both the MS and SE (see Materials and Methods) for each of the 295 subjects and characterized the brain states of each subject with points in the MS vs. SE phase plane, as seen in the top panel of Fig. 2 **a**. We found that the value for MS from these subjects extended from 0.2 to 0.7, and the distribution of subjects was not even but exhibited a greater tendency to the low MS range (Fig. 2 **a**, low panel). This result suggested that even in the resting state, there is significant variability among the subjects' brain states. It is clearly seen that these state points formed an inverted-U trajectory in the phase plane. The SE exhibited a maximum at the moderate value of MS, which implied the existence of a state with dynamic richness between order and disorder. We performed a phase randomization method on the fMRI data and found that this inverted-U curve disappeared in the randomized surrogate datasets (size=500, identified by visual inspection; examples can be seen in Fig. S1). Therefore, we argue that this inverted-U curve reflected a special spatiotemporal structure of brain dynamics that did not exist in randomized data. In fact, several previous studies have suggested that moderate synchrony with maximal variability co-occurs with critical dynamics; this can be observed at the cellular network level with multiple electrode recording (MER) techniques or at the cortical regional level with EEG[9,12]. To verify this point in our study, we applied avalanche size analysis to calculate the branching parameter σ for each subject. We found that with increasing MS, the branching parameter increased from less than 1 to higher than 1, crossing 1 at a moderate value of MS (Fig. 2 **b**).

Furthermore, we selected three groups from the above subjects: the low synchronization group (LMS group; the 20 most left subjects in Fig. 2 **a** with an MS value of $\langle r \rangle = 0.2824 \pm 0.0219$), the moderate synchronization group (MMS group; the 20 subjects located near the peak of curve in Fig. 2 **a** with an MS value of $\langle r \rangle = 0.5041 \pm 0.0042$), and the high synchronization group (HMS group; the 20 most right subjects in Fig. 2 **a** with an MS value of $\langle r \rangle = 0.6304 \pm 0.0246$). For each group, we performed avalanche distribution analysis to identify which group was closest to the critical point (Fig. 2 **c**-**f**). After obtaining scaling exponents α and τ for each group with a threshold of 1.4 SD (Fig. 2 **c** and **d**), the scaling relationship showed the best match for the MMS group (Fig. 2 **e**), and more detailed analysis results can be found in Fig. S2 in the Supplementary Materials. We also calculated κ, an often used parameter that could distinguish the difference between data and the theoretically suggested power-law distribution[10,11,19,66,67]. As shown in Fig. 2 **f**, as the discrete bin number m increases, the κ values become stable. The stabilized κ is smaller than 1 for the LMS group but larger than 1 for the HMS and MMS groups. The κ value for the MMS group was closest to 1. Therefore, the above results suggested that subjects' brains with moderate MS and maximal SE are poised closest to the critical point, evidenced by consistent hallmarks of criticality. On the other hand, the large dispersion of subjects among the phase space between asynchronous (subcritical) and synchronous (supercritical) states also provides an opportunity to investigate the phase transition in brains.

2 The complexity in the FC network is maximized by criticality

Since the phase transition similar to those in physics systems could be observed, we investigated how this phase transition could impact the organization of FC networks. For convenience, we used MS to indicate this transition. Fig. 3 **a** demonstrates the dependence of mean FC on MS for each subject. It was seen that the mean FC increased monotonically from the subcritical to supercritical state. This result is comprehensible because for two oscillatory time series, the linear Pearson correlation

is also a measure of synchrony between them.

Next, we assessed how the variousness in FC strength changes as the brain undergoes a phase transition from the sub- to supercritical states. We used FC entropy and FC diversity as measures of variousness in FC strength in the brain networks. FC entropy is a direct measure of Shannon entropy from the probability distribution of FC strength obtained from the FC matrix, whereas FC diversity measures the similarity between the distribution of real FC matrix elements and uniform distribution. In previous studies, the former had been associated with healthy aging[63], and the latter is predicted to be maximized at the critical point by a computer model with Ginzburg-Landau equations[32]. We found that both FC entropy (Fig. 3 **b**) and FC diversity (Fig. 3 **c**) peaked at the moderate value of MS; however, the peak position for these two measures was more rightward than that of SE.

The flexibility in dynamic FC reflects the extent of abundant connection patterns among regions and how frequent switching may occur between different patterns. In this work, we adopted the connection number entropy as a measure of flexibility in FC networks. Our previous study showed that this measure was maximized at the critical point in a large-scale brain network model that combined DTI structural data and excitable cellular automaton[33], and this measure could be reduced in the brains of patients with moyamoya disease[68]. In this study, we found that the flexibility in FC was maximized with a moderate value of MS (Fig. 3 **d**). The maximization was robust in a wide range of THR_{FC} thresholds and sliding window lengths (Fig. S3). This result supported our previous conclusion[33,68]. Compared with FC entropy and FC diversity, the peak position for FC flexibility was nearer to the critical point.

FC entropy, diversity, and flexibility are often used in resting-state fMRI studies to measure the complexity in the structure and dynamic reconfiguration of FC networks. Here, the study suggested that the complexity in FC networks is maximized by criticality.

3 The maximized structure-function coupling around the critical point

From the obtained FC matrix and SC matrix for each subject, we constructed FC networks for each subject and a group-aggregated SC network. We used THR_{FC} and THR_{SC} to control the link density in the FC networks and SC network, respectively. We measured the similarity between the FC network for each subject and the group-aggregate SC network with Pearson correlation and Hamming distance. Fig. 4 **a** and **b** demonstrate the dependence of similarity on the MS of each subject with a link density of 0.7 in the FC networks. The similarity between FC and SC was maximal for subjects with moderate synchrony, as the Pearson correlation was maximized (Fig. 4 **a**), while the Hamming distance was minimized (Fig. 4 **b**) for these subjects. This maximization of similarity in FC and SC could be observed in a wide range of link densities in the FC and SC networks. To further consolidate the above results, we measured the similarity between FC and SC for the three groups defined above as a function of FC network link density. Fig. 4 **c** and **d** show that as the link density increased, the correlation coefficient between the FC and SC matrices first increased and then decreased, and consistently, the Hamming distance exhibited the opposite tendency. When the FC link density was large, the MMS group showed a significantly higher correlation and a lower Hamming distance between the FC and SC networks than the other two groups. Similarly, by varying THR_{SC}, we found that the maximized similarity in FC and SC at the critical point was robust in the wide range of link densities in the SC network (Figs. S5 and S6).

We noticed that for a large link density of FC, the dependence of similarity on link density monotonically decreased (Fig. 4 **c** and **d;** Fig. S4 **a** and **b**). Since lower link density conserved only stronger links in FC networks, we deduced that structural connections were mostly reflected in the strong functional connections. Meanwhile, the similarity also decreased as the threshold for THR_{SC} in SC networks decreased (Fig. S5), suggesting that the structural connections that were mostly reflected in the

functional connection were those shared by most subjects because structural connections specified to individuals would be excluded with high THR_{SC}.

4 The dynamic phase transition in individual subjects' brains

The observed individual brain states dispersed around the critical point provided an opportunity to investigate the dynamic phase transition in individual brains. To this end, for the LMS, MMS, and HMS groups defined above, we randomly selected two subjects from each group. We calculated the instantaneous MS $\langle r \rangle_n$ and SE $\mathrm{H}(r)_n$ for these six subjects with the sliding window approach (Fig. 5 **a**, s1-s6) from their Kuramoto order parameter parameters $r(t)$ (Fig. 5 **b**). We observed a time-dependent change in individuals' brain states in the state space following the inverted-U trajectory, as shown in the top panel of Fig. 2 **a**. In the time period limited by scan duration, we observed that subjects who were farther away from the critical point tended to stay in the regime decided by MS, and events of crossing the critical point (black lines at $r(t) = 0.5$) to the other regime seldom occurred (s1, s2, s5, and s6 in Fig. 5 **a**, or Fig. 5 **b**, top and bottom panel). Subjects who were nearer the critical point were more likely to cross the critical point, which resembled the phase transitions in physics systems (s3 and s4 in Fig. 5 **a**, or Fig. 5 **b**, middle panel).

To validate the above observation at the population level, we divided the 295 subjects at hand into eight groups with different levels of synchrony and calculated the corresponding probability distribution of the Kuramoto order parameter $r(t)$. It is seen clearly from Fig. 5 **c** that as the synchrony level decreases, the distribution of the Kuramoto order parameter becomes narrow and less tilted. Meanwhile, we found that the dwell time, which referred to the time interval between two successive critical point crossing events, exhibited heavier tails in its distribution for low synchrony groups (Fig. 5 **d**). These results implied the higher inertness in the subcritical regime than others, and brains were more likely to stay in this regime with longer dwell time.

Next, we calculated the distribution of vertical and horizontal moving distances $\Delta\langle r \rangle_n$

and $\Delta \mathrm{H}(r)_n$ in state space in a fixed time interval Δn (the time points or volumes of one step of the sliding window) for all subjects. We found that the distribution of vertical and horizontal moving distances were both symmetrical with a mean of zero (Fig. 5 **e** and **f**), suggesting that the inverted-U trajectory in the state space was stable and unlikely to change its shape as time progressed. Furthermore, the position ($\langle r \rangle$) dependent velocity distribution is maximal for horizontal velocity ($\frac{\langle |\Delta \langle r \rangle_n| \rangle}{\Delta n}$) and minimal for vertical velocity ($\frac{\langle |\Delta \langle r \rangle_n| \rangle}{\Delta n}$) near the critical point. The maximal horizontal velocity around the critical point implied that at this point, the systems were most sensitive to the perturbations due to internal fluctuations or external modulations. Meanwhile, the lower vertical and horizontal velocities in the subcritical regime compared to the supercritical regime also reflected the high inertness in the subcritical regime.

It was of interest to determine if the maximization of FC complexity, as well as function-structure coupling, around the critical point could be realized dynamically when the individual brains endured phase transition. To this end, we obtained the time-dependent FC matrices with the sliding window method and calculated FC entropy (Fig. 6 **a**), FC diversity (Fig. 6 **b**), and two measures for similarity between FC and SC (Fig. 6 **c** and **d**) as a function of instantaneous MS in each time window. The time-dependent complexity and similarity measures followed almost the exact trajectories as those in the static measurements shown in Fig. 3 **b** and **c**, as well as Fig. 4 **a** and **b**. This result implied that FC complexity and similarity between FC and SC were indeed modulated by phase transition in brains, and their maximization could be realized dynamically by positioning the system around the critical point.

5 High fluid intelligence and working memory capacity were associated with critical dynamics

Another important prediction from the critical brain hypothesis is that brains that are closer to criticality should be better in cognitive performance. Here, we assessed

linear relationships between SE and intelligence scores of the available subjects. We found that SE values were significantly correlated with fluid intelligence scores (PMAT; Fig. 7 **a**) but not with crystallized intelligence scores (picture vocabulary; Fig. 7 **b**). Meanwhile, we found that working memory scores, which were assessed using the Listing Sorting Working Memory test from the NIH Toolbox, were significantly correlated with SE (List sorting; Fig. 7 **c**). We also noted here that these scores were significantly correlated with many other measures that were found to be maximized at the critical point, namely, FC entropy, FC diversity, and FC flexibility (Fig. S7 in Supplementary Materials). Meanwhile, there were significant quadratic functions between MS and fluid intelligence and working memory scores but not crystallized intelligence scores (Fig. 7 **d-f**). Therefore, it was clear that brains that were closer to criticality were associated with higher fluid intelligence and working memory scores.

Since a wide variety of experiments have demonstrated that fluid intelligence is associated with a distributed network of regions in the frontal and parietal cortices, including the dorsal lateral prefrontal cortex, superior parietal lobe, and supramarginal gyrus[41,69], we decided to find more relationship between these regions with critical dynamics indicated by maximized SE. To obtain the relevant regions in a fine-grained division of the brain, we adopted the Human Brainnetome Atlas, which contains 210 cortical and 36 subcortical subregions[70]. We extracted from each brain region the voxel-wise BOLD signals and calculated the regional SE for these 246 regions. We found that regions whose SE exhibited significant positive correlation with PMAT scores were located in the bilateral middle frontal, inferior frontal, and orbitofrontal parts in prefrontal cortex, as well as right supramarginal gyrus in the parietal lobe ($p<0.05$, FDR corrected; Table 1).

Discussion

In this study, we introduced a novel yet simple method to uncover the criticality and phase transition of brain dynamics through resting-state fMRI data analysis. With this method, the available subjects were mapped into a trajectory where the critical point,

as well as sub- and supercritical regimes divided by the critical point, could be identified. These results supported critical brain theory with avalanche criticality under the second-order phase transition. We demonstrated that the complexity in brain FC was maximized around the critical point, as was the structure-function coupling. Therefore, our findings validated two predictions of criticality in large-scale networks. Then, we observed a dynamic phase transition in individual subjects' brains and found that the brains tended to stay in the subcritical brains, indicated by a longer dwell time in this region. Finally, we found that high fluid intelligence and working memory capacity were associated with critical dynamics rather than noncritical dynamics, not only globally but also regionally, suggesting the functional advantages of critical dynamics in resting-state brains.

Functional segregation and functional integration is a central organizing principle of the cerebral cortex. It has been argued that FC complexity characterizes the interplay of functional segregation and functional integration[71]. A comparison between simulated and empirically obtained resting-state FC indicates that the human brain at rest, lies in a dynamic state that reflects the largest complexity its anatomical connectome can host[72]. Recently, many studies have tried to link complexity with cognitive performance, human intelligence, and even consciousness either measured by Φ (big phi) in integrated information theory or discriminated between levels of sedation[28,73-75]. Meanwhile, there is a growing awareness that complexity is strongly related to criticality. A recent study showed that criticality maximized complexity in dissociated hippocampal cultures produced from rats[26]. Here, in this study, we measured FC complexity from different perspectives, either on its strength diversity or on its dynamic flexibility (Fig.3 **b-d**). With the observation of the phase transition trajectory, we demonstrated that these measures of FC complexity were maximized around the critical point. Therefore, the formulation that criticality maximizes complexity was evidenced in our work empirically with fMRI data at the whole-brain network level.

It has been shown that human brains possess a stable set of functionally coupled

networks that echo many known features of anatomical organization[76]. Several computational modeling studies have demonstrated that critical dynamics could best explore the repertoire provided by the structural connectome[23,77]. Recent studies also suggested the capacity of repertoire provided by the structural connectome could be extend by the hierarchical modular structural organization[32]. Therefore, the structure-function coupling was believed to be at its maximal as the system is at criticality[32], and it could be disrupted by losing of criticality[78], or disruption of hierarchical organization of structural networks. Previous study in anesthetized human brains has found structure-function decoupling accompanied by unidirectional departure from a critical point[23]. Actually, the FC flexibility could be considered as a measure of the extent the FC explores the repertoire provided by structural connectome, and the highest FC flexibility occurs when the system is at criticality[33] (Fig.3 **d**). Our work demonstrated the maximal exploration of structural connections at the critical point do happens in resting state brains (Fig. 4). However, since we used the grouply aggregated structural connection networks, we did not investigate how organization of structural connections could impact on the capacity of network repertoire. This issue will be investigated in the future.

Interestingly, although the brain hovers around the critical point, the brain prefers to stay in the subcritical region, as the subject distribution was skewed toward a disordered state, and the dwell time in the subcritical state was longer (Fig. 5). Previous analysis of *in vivo* data has argued that the mammalian brain self-organizes to a slightly subcritical regime[18]. It was suggested that operating in a slightly subcritical regime may prevent the brain from tipping over to supercriticality, which has been linked to epilepsy. Meanwhile, with a slightly subcritical regime deviates only little from criticality, the computational capabilities may still be close to optimal. However, our results showed that the resting state brains could actually stay in the supercritical regimes. So the preference of brains for subcritical regime may not because of prevention of too ordered states. In another study, by relating the EEG-domain cascades to spatial BOLD patterns in simultaneously recorded fMRI

data, the researchers found that while resting-state cascades were associated with an approximate power-law form, the task state was associated with subcritical dynamics[19]. They argued that while a high dynamic range and a large repertoire of brain states may be advantageous for the resting state with near-critical dynamics, a lower dynamic range may reduce elements of interference affecting task performance in a focused cognitive task with subcritical dynamics[19]. Therefore, there remains a possibility that the resting state is not "pure resting state", but mixed with some occasional "task state" for some subjects. However, further delicately designed experimental studies are required to test this conjecture. Anyway, it is interesting to uncover the relationship between cognitive state and neural dynamics that lies on a spectrum. Our method proposed in this study could be useful in future studies on this topic.

Recently, Ezaki et al. used the Ising model to map BOLD signals on a two-dimensional phase space and found that human fMRI data were in the paramagnetic phase and were close to the boundary with the spin-glass phase but not to the boundary with the ferromagnetic phase[79]. Since the spin-glass phase usually yields chaotic dynamics whereas the ferromagnetic phase is obviously nonchaotic, their results suggested that the brain is around the "edge of chaos criticality" instead of "avalanche criticality". However, our findings suggest that avalanche criticality does occur in large-scale brain networks. Therefore, it is interesting to investigate if both kinds of criticality could co-occur in large-scale brain networks[37]. On the other hand, Ezaki et al. also found that criticality of brain dynamics was associated with human fluid intelligence, though they used performance IQ to reflect fluid intelligence, which refers to active or effortful problem solving and maintenance of information. In our work, we assessed the correlation between fluid intelligence and the critical dynamics indicated by synchronization entropy for brain regions, and found regions showed significant positive correlations were located in prefrontal and inferior parietal cortex (Fig. 8). These two regions were most frequently reported in studies of intelligence and its biological basis, including structural neuroimaging studies using

voxel-based morphometry, magnetic resonance spectroscopy, and DTI, as well as functional imaging studies using positron emission tomography (PET) or fMRI[41]. Also, in the P-FIT theory of intelligence, these two regions are considered as the most crucial nodes of the brain network underlying human intelligence[41,69]. However, we didn't find significant correlations between critical dynamics and fluid intelligence performance in other areas within the P-FIT network, such as superior parietal lobule, the anterior cingulate and regions within the temporal and occipital lobes. Future studies on the interactions between these nodes with the consideration of critical dynamics may provide further insight into the neural dynamic basis of human intelligence.

Our study suggested that not only fluid intelligence but also working memory capacity was associated with critical dynamics. This is possibly because working memory may share the same capacity constraint through similar neural networks with fluid intelligence[80-82]. In our study, the critical dynamics in the prefrontal and inferior parietal cortex also exhibited high correlation with working memory capacity (Fig. S8 and Table S1). Furthermore, it has been well established that working memory is strongly modulated by dopamine, and too strong or too weak dopamine D1 activation is detrimental for working memory, with the optimal performance achieved at an intermediate level[83,84]. Recent studies on neural network models have shown that the optimal performance of WM co-occurs with critical dynamics at the network level and the excitation/inhibition balance at the level of individual neurons and is modulated by dopamine at the synaptic level through a series of U or inverted-U profiles[85]. Here in this study, we demonstrated that the optimal performance of working memory and criticality co-occurs at the system level.

Conclusions

In conclusion, we proposed a simple approach to map individuals' brain dynamics from resting-state fMRI scans on the phase transition trajectory and identify subjects

who are close to the critical point. With this approach, we validated two predictions of critical brain hypothesis on large scale brain networks, i.e., maximized FC complexity and maximized structure-function coupling around the critical point. We also observed the tendency of brain to stay in subcritical regime. Finally, we found that the critical dynamics in large-scale brain networks were associated with high scores in fluid intelligence and working memory, implying the vital role of large scale critical dynamics in cognitive performance. We also identified key brain regions whose critical dynamics was highly correlated with human intelligence. Our findings fit with critical brain hypothesis that optimal neural computation is optimized by critical brain dynamics hallmarked by scale-free avalanche activity, and could provide a solution for improving the effects of future interventions targeting aspects of cognitive decline[86], possibly by control the criticality through non-invasive stimulation[87].

References

1 Hesse, J. & Gross, T. Self-organized criticality as a fundamental property of neural systems. *Front Syst Neurosci* **8**, 166-166, doi:10.3389/fnsys.2014.00166 (2014).

2 Cocchi, L., Gollo, L. L., Zalesky, A. & Breakspear, M. Criticality in the brain: A synthesis of neurobiology, models and cognition. *Progress in Neurobiology* **158**, 132-152, doi:https://doi.org/10.1016/j.pneurobio.2017.07.002 (2017).

3 Gal, A. & Marom, S. Self-organized criticality in single-neuron excitability. *Physical Review E* **88**, 062717, doi:10.1103/PhysRevE.88.062717 (2013).

4 Solovey, G., Miller, K., Ojemann, J., Magnasco, M. & Cecchi, G. Self-Regulated Dynamical Criticality in Human ECoG. *Frontiers in Integrative Neuroscience* **6**, 44 (2012).

5 Plenz, D. Neuronal avalanches and coherence potentials. *The European Physical Journal Special Topics* **205**, 259-301, doi:10.1140/epjst/e2012-01575-5 (2012).

6 Tagliazucchi, E., Balenzuela, P., Fraiman, D. & Chialvo, D. Criticality in Large-Scale Brain fMRI Dynamics Unveiled by a Novel Point Process Analysis. *Frontiers in Physiology* **3**, 15 (2012).

7 Shriki, O. *et al.* Neuronal avalanches in the resting MEG of the human brain. *The Journal of neuroscience : the official journal of the Society for Neuroscience* **33**, 7079-7090, doi:10.1523/JNEUROSCI.4286-12.2013 (2013).

8 Beggs, J. M. & Plenz, D. Neuronal avalanches in neocortical circuits. *The Journal of neuroscience : the official journal of the Society for Neuroscience* **23**, 11167-11177, doi:10.1523/JNEUROSCI.23-35-11167.2003 (2003).

9 Meisel, C., Olbrich, E., Shriki, O. & Achermann, P. Fading Signatures of Critical Brain Dynamics during Sustained Wakefulness in Humans. *The Journal of Neuroscience* **33**, 17363, doi:10.1523/JNEUROSCI.1516-13.2013 (2013).

10 Shew, W. L., Yang, H., Yu, S., Roy, R. & Plenz, D. Information capacity and transmission are maximized in balanced cortical networks with neuronal avalanches. *The Journal of neuroscience : the official journal of the Society for Neuroscience* **31**, 55-63, doi:10.1523/JNEUROSCI.4637-10.2011 (2011).

11 Shew, W. L., Yang, H., Petermann, T., Roy, R. & Plenz, D. Neuronal Avalanches Imply Maximum Dynamic Range in Cortical Networks at Criticality. *The Journal of Neuroscience* **29**, 15595, doi:10.1523/JNEUROSCI.3864-09.2009 (2009).

12 Yang, H., Shew, W. L., Roy, R. & Plenz, D. Maximal Variability of Phase Synchrony in Cortical Networks with Neuronal Avalanches. *The Journal of Neuroscience* **32**, 1061, doi:10.1523/JNEUROSCI.2771-11.2012 (2012).

13 Shew, W. L. & Plenz, D. The Functional Benefits of Criticality in the Cortex. *The Neuroscientist* **19**, 88-100, doi:10.1177/1073858412445487 (2012).

14 Beggs, J. & Timme, N. Being Critical of Criticality in the Brain. *Frontiers in Physiology* **3**, 163 (2012).

15 Touboul, J. & Destexhe, A. Can power-law scaling and neuronal avalanches arise from stochastic dynamics? *PloS one* **5**, e8982-e8982, doi:10.1371/journal.pone.0008982 (2010).

16 Fontenele, A. J. *et al.* Criticality between Cortical States. *Phys Rev Lett* **122**, 208101, doi:10.1103/PhysRevLett.122.208101 (2019).

17 Scott, G. *et al.* Voltage Imaging of Waking Mouse Cortex Reveals Emergence of Critical Neuronal Dynamics. *The Journal of Neuroscience* **34**, 16611, doi:10.1523/JNEUROSCI.3474-14.2014 (2014).

18 Priesemann, V. *et al.* Spike avalanches in vivo suggest a driven, slightly subcritical brain state. *Front Syst Neurosci* **8**, 108-108, doi:10.3389/fnsys.2014.00108 (2014).

19 Fagerholm, E. D. *et al.* Cascades and cognitive state: focused attention incurs subcritical dynamics. *The Journal of neuroscience : the official journal of the Society for Neuroscience* **35**, 4626-4634, doi:10.1523/JNEUROSCI.3694-14.2015 (2015).

20 He, B. J. Scale-free properties of the functional magnetic resonance imaging signal during rest and task. *The Journal of neuroscience : the official journal of the Society for Neuroscience* **31**, 13786-13795, doi:10.1523/JNEUROSCI.2111-11.2011 (2011).

21 Karahanoğlu, F. I. & Van De Ville, D. Dynamics of large-scale fMRI networks: Deconstruct brain activity to build better models of brain function. *Current Opinion in Biomedical Engineering* **3**, 28-36, doi:https://doi.org/10.1016/j.cobme.2017.09.008 (2017).

22 Lee, H. *et al.* Relationship of critical dynamics, functional connectivity, and states of consciousness in large-scale human brain networks. *NeuroImage* **188**, 228-238, doi:https://doi.org/10.1016/j.neuroimage.2018.12.011 (2019).

23 Tagliazucchi, E. *et al.* Large-scale signatures of unconsciousness are consistent with a departure from critical dynamics. *Journal of the Royal Society, Interface* **13**, 20151027-20151027, doi:10.1098/rsif.2015.1027 (2016).

24 Tagliazucchi, E. & Chialvo, D. R. Brain complexity born out of criticality. *AIP Conference Proceedings* **1510**, 4-13, doi:10.1063/1.4776495 (2013).

25 Popiel, N. J. K., S.; Abeyasinghe, P.M.; Riganello, F.; Nichols, E.S.; Owen, A.M.; Soddu, A. The Emergence of Integrated Information, Complexity, and 'Consciousness' at Criticality. *Entropy* **22** (2020).

26 Timme, N. M. *et al.* Criticality Maximizes Complexity in Neural Tissue. *Frontiers in physiology* **7**, 425-425, doi:10.3389/fphys.2016.00425 (2016).

27 Omidvarnia, A., Zalesky, A., Van De Ville, D., Jackson, G. D. & Pedersen, M. Temporal complexity of fMRI is reproducible and correlates with higher order cognition. *bioRxiv*, 770826, doi:10.1101/770826 (2019).

28 Ahmadlou, M., Adeli, A., Bajo, R. & Adeli, H. Complexity of functional connectivity networks in mild cognitive impairment subjects during a working memory task. *Clinical Neurophysiology* **125**, 694-702, doi:https://doi.org/10.1016/j.clinph.2013.08.033 (2014).

29 Wang, B. *et al.* Decreased Complexity in Alzheimer's Disease: Resting-State fMRI Evidence of Brain Entropy Mapping. *Front Aging Neurosci* **9**, 378-378, doi:10.3389/fnagi.2017.00378 (2017).

30 Smyser, C. D. *et al.* Resting-State Network Complexity and Magnitude Are Reduced in Prematurely Born Infants. *Cerebral cortex (New York, N.Y. : 1991)* **26**, 322-333, doi:10.1093/cercor/bhu251 (2016).

31 Anokhin, A. P., Birbaumer, N., Lutzenberger, W., Nikolaev, A. & Vogel, F. Age increases brain complexity. *Electroencephalography and Clinical Neurophysiology* **99**, 63-68, doi:https://doi.org/10.1016/0921-884X(96)95573-3 (1996).

32 Wang, R. *et al.* Hierarchical Connectome Modes and Critical State Jointly Maximize Human Brain Functional Diversity. *Physical Review Letters* **123**, 038301, doi:10.1103/PhysRevLett.123.038301 (2019).

33 Song, B. *et al.* Maximal flexibility in dynamic functional connectivity with critical dynamics revealed by fMRI data analysis and brain network modelling. *Journal of Neural Engineering* **16**, 056002, doi:10.1088/1741-2552/ab20bc (2019).

34 Nakagawa, T. T., Jirsa, V. K., Spiegler, A., McIntosh, A. R. & Deco, G. Bottom up modeling of the connectome: Linking structure and function in the resting brain and their changes in aging. *NeuroImage* **80**, 318-329, doi:https://doi.org/10.1016/j.neuroimage.2013.04.055 (2013).

35 Deco, G., Jirsa, V. K. & McIntosh, A. R. Emerging concepts for the dynamical organization of resting-state activity in the brain. *Nature Reviews Neuroscience* **12**, 43-56, doi:10.1038/nrn2961 (2011).

36 Scarpetta, S., Apicella, I., Minati, L. & de Candia, A. Hysteresis, neural avalanches, and critical behavior near a first-order transition of a spiking neural network. *Physical Review E* **97**, 062305, doi:10.1103/PhysRevE.97.062305 (2018).

37 Kanders, K., Lorimer, T. & Stoop, R. Avalanche and edge-of-chaos criticality do not necessarily co-occur in neural networks. *Chaos: An Interdisciplinary Journal of Nonlinear Science* **27**, 047408, doi:10.1063/1.4978998 (2017).

38 Hobbs, J. P., Smith, J. L. & Beggs, J. M. Aberrant Neuronal Avalanches in Cortical Tissue Removed From Juvenile Epilepsy Patients. *Journal of Clinical Neurophysiology* **27** (2010).

39 Meisel, C., Storch, A., Hallmeyer-Elgner, S., Bullmore, E. & Gross, T. Failure of Adaptive Self-Organized Criticality during Epileptic Seizure Attacks. *PLOS Computational Biology* **8**, e1002312, doi:10.1371/journal.pcbi.1002312 (2012).

40 Kanders, K., Lee, H., Hong, N., Nam, Y. & Stoop, R. Fingerprints of a second order critical line in developing neural networks. *Communications Physics* **3**, 13, doi:10.1038/s42005-019-0276-8 (2020).

41 Jung, R. E. & Haier, R. J. The Parieto-Frontal Integration Theory (P-FIT) of intelligence: Converging neuroimaging evidence. *Behavioral and Brain Sciences* **30**, 135-154, doi:10.1017/S0140525X07001185 (2007).

42 Van Essen, D. C. *et al.* The WU-Minn Human Connectome Project: an overview. *NeuroImage* **80**, 62-79, doi:10.1016/j.neuroimage.2013.05.041 (2013).

43 Glasser, M. F. *et al.* The minimal preprocessing pipelines for the Human Connectome Project. *NeuroImage* **80**, 105-124, doi:https://doi.org/10.1016/j.neuroimage.2013.04.127 (2013).

44 Glasser, M. F. *et al.* The Human Connectome Project's neuroimaging approach. *Nature neuroscience* **19**, 1175-1187, doi:10.1038/nn.4361 (2016).

45 Smith, S. M. *et al.* A positive-negative mode of population covariation links brain connectivity, demographics and behavior. *Nature Neuroscience* **18**, 1565-1567, doi:10.1038/nn.4125 (2015).

46 Sotiropoulos, S. N. *et al.* Advances in diffusion MRI acquisition and processing in the Human Connectome Project. *NeuroImage* **80**, 125-143, doi:10.1016/j.neuroimage.2013.05.057 (2013).

47 Yeh, F.-C. & Tseng, W.-Y. I. NTU-90: A high angular resolution brain atlas constructed by q-space diffeomorphic reconstruction. *NeuroImage* **58**, 91-99, doi:https://doi.org/10.1016/j.neuroimage.2011.06.021 (2011).

48 Yeh, F., Wedeen, V. J. & Tseng, W. I. Generalized ${ q}$-Sampling Imaging. *IEEE Transactions on Medical Imaging* **29**, 1626-1635, doi:10.1109/TMI.2010.2045126 (2010).

49 Yeh, F.-C., Liu, L., Hitchens, T. K. & Wu, Y. L. Mapping immune cell infiltration using restricted diffusion MRI. *Magnetic Resonance in Medicine* **77**, 603-612, doi:10.1002/mrm.26143 (2017).

50 Yeh, F.-C., Verstynen, T. D., Wang, Y., Fernández-Miranda, J. C. & Tseng, W.-Y. I. Deterministic Diffusion Fiber Tracking Improved by Quantitative Anisotropy. *PLOS ONE* **8**, e80713, doi:10.1371/journal.pone.0080713 (2013).

51 Barch, D. M. *et al.* Function in the human connectome: task-fMRI and individual differences in behavior. *NeuroImage* **80**, 169-189, doi:10.1016/j.neuroimage.2013.05.033 (2013).

52 Hearne, L. J., Mattingley, J. B. & Cocchi, L. Functional brain networks related to individual differences in human intelligence at rest. *Scientific Reports* **6**, 32328, doi:10.1038/srep32328 (2016).

53 Bilker, W. B. *et al.* Development of Abbreviated Nine-Item Forms of the Raven's Standard Progressive Matrices Test. *Assessment* **19**, 354-369, doi:10.1177/1073191112446655 (2012).

54 Wendelken, C., Nakhabenko, D., Donohue, S. E., Carter, C. S. & Bunge, S. A. "Brain Is to Thought as Stomach Is to ??": Investigating the Role of Rostrolateral Prefrontal Cortex in Relational Reasoning. *Journal of Cognitive Neuroscience* **20**, 682-693, doi:10.1162/jocn.2008.20055 (2007).

55 Prichard, D. & Theiler, J. Generating surrogate data for time series with several simultaneously measured variables. *Physical Review Letters* **73**, 951-954, doi:10.1103/PhysRevLett.73.951 (1994).

56 Bocaccio, H. *et al.* The avalanche-like behaviour of large-scale haemodynamic activity from wakefulness to deep sleep. *Journal of The Royal Society Interface* **16**, 20190262, doi:10.1098/rsif.2019.0262 (2019).

57 Friedman, N. *et al.* Universal Critical Dynamics in High Resolution Neuronal Avalanche Data. *Physical Review Letters* **108**, 208102, doi:10.1103/PhysRevLett.108.208102 (2012).

58 Sethna, J. P., Dahmen, K. A. & Myers, C. R. Crackling noise. *Nature* **410**, 242-250, doi:10.1038/35065675 (2001).

59 Touboul, J. & Destexhe, A. Power-law statistics and universal scaling in the absence of criticality. *Physical Review E* **95**, 012413, doi:10.1103/PhysRevE.95.012413 (2017).

60 Clauset, A., Shalizi, C. R. & Newman, M. E. J. Power-Law Distributions in Empirical Data. *SIAM Review* **51**, 661-703 (2009).

61 Marshall, N. *et al.* Analysis of Power Laws, Shape Collapses, and Neural Complexity: New Techniques and MATLAB Support via the NCC Toolbox. *Frontiers in Physiology* **7**, 250 (2016).

62 Deluca, A. & Corral, Á. Fitting and goodness-of-fit test of non-truncated and truncated power-law distributions. *Acta Geophysica* **61**, 1351-1394, doi:10.2478/s11600-013-0154-9 (2013).

63 Yao, Y. *et al.* The Increase of the Functional Entropy of the Human Brain with Age. *Scientific Reports* **3**, 2853, doi:10.1038/srep02853 (2013).

64 Harris, T. E. The theory of branching process. *New York: Dover*.

65 Zapperi, S., Lauritsen, K. B. & Stanley, H. E. Self-Organized Branching Processes: Mean-Field Theory for Avalanches. *Physical Review Letters* **75**, 4071-4074, doi:10.1103/PhysRevLett.75.4071 (1995).

66 Poil, S.-S., Hardstone, R., Mansvelder, H. D. & Linkenkaer-Hansen, K. Critical-State Dynamics of Avalanches and Oscillations Jointly Emerge from Balanced Excitation/Inhibition in Neuronal Networks. *The Journal of Neuroscience* **32**, 9817, doi:10.1523/JNEUROSCI.5990-11.2012 (2012).

67 Palva, J. M. *et al.* Neuronal long-range temporal correlations and avalanche dynamics are correlated with behavioral scaling laws. *Proc Natl Acad Sci U S A* **110**, 3585-3590, doi:10.1073/pnas.1216855110 (2013).

68 Lei, Y. *et al.* Reconfigured functional network dynamics in adult moyamoya disease: a resting-state fMRI study. *Brain Imaging and Behavior* **14**, 715-727, doi:10.1007/s11682-018-0009-8 (2020).

69 Nikolaidis, A. *et al.* Multivariate Associations of Fluid Intelligence and NAA. *Cerebral Cortex* **27**, 2607-2616, doi:10.1093/cercor/bhw070 (2017).

70 Fan, L. *et al.* The Human Brainnetome Atlas: A New Brain Atlas Based on Connectional Architecture. *Cerebral Cortex* **26**, 3508-3526, doi:10.1093/cercor/bhw157 (2016).

71 Sporns, O. Network attributes for segregation and integration in the human brain. *Current Opinion in Neurobiology* **23**, 162-171, doi:https://doi.org/10.1016/j.conb.2012.11.015 (2013).

72 Tononi, G., Sporns, O. & Edelman, G. M. A measure for brain complexity: relating functional segregation and integration in the nervous system. *Proceedings of the National Academy of Sciences* **91**, 5033, doi:10.1073/pnas.91.11.5033 (1994).

73 Tononi, G., Edelman, G. M. & Sporns, O. Complexity and coherency: integrating information in the brain. *Trends in Cognitive Sciences* **2**, 474-484, doi:10.1016/S1364-6613(98)01259-5 (1998).

74 Saxe, G. N., Calderone, D. & Morales, L. J. Brain entropy and human intelligence: A resting-state fMRI study. *PLOS ONE* **13**, e0191582, doi:10.1371/journal.pone.0191582 (2018).

75 Duncan, J., Chylinski, D., Mitchell, D. J. & Bhandari, A. Complexity and compositionality in fluid intelligence. *Proceedings of the National Academy of Sciences* **114**, 5295, doi:10.1073/pnas.1621147114 (2017).

76 Krienen, F. M., Yeo, B. T. T. & Buckner, R. L. Reconfigurable task-dependent functional coupling modes cluster around a core functional architecture. *Philos Trans R Soc Lond B Biol Sci* **369**, 20130526, doi:10.1098/rstb.2013.0526 (2014).

77 Deco, G. & Jirsa, V. K. Ongoing Cortical Activity at Rest: Criticality, Multistability, and Ghost Attractors. *The Journal of Neuroscience* **32**, 3366, doi:10.1523/JNEUROSCI.2523-11.2012 (2012).

78 Cocchi, L. *et al.* Disruption of structure–function coupling in the schizophrenia connectome. *NeuroImage: Clinical* **4**, 779-787, doi:https://doi.org/10.1016/j.nicl.2014.05.004 (2014).

79 Ezaki, T., Fonseca dos Reis, E., Watanabe, T., Sakaki, M. & Masuda, N. Closer to critical resting-state neural dynamics in individuals with higher fluid intelligence. *Communications Biology* **3**, 52, doi:10.1038/s42003-020-0774-y (2020).

80 Jaeggi, S. M., Buschkuehl, M., Jonides, J. & Perrig, W. J. Improving fluid intelligence with training on working memory. *Proceedings of the National Academy of Sciences* **105**, 6829, doi:10.1073/pnas.0801268105 (2008).

81 Halford, G. S., Cowan, N. & Andrews, G. Separating cognitive capacity from knowledge: a new hypothesis. *Trends in cognitive sciences* **11**, 236-242, doi:10.1016/j.tics.2007.04.001 (2007).

82 Kane, M. J. & Engle, R. W. The role of prefrontal cortex in working-memory capacity, executive attention, and general fluid intelligence: An individual-differences perspective. *Psychonomic Bulletin & Review* **9**, 637-671, doi:10.3758/BF03196323 (2002).

83 Zahrt, J., Taylor, J. R., Mathew, R. G. & Arnsten, A. F. Supranormal stimulation of D1 dopamine receptors in the rodent prefrontal cortex impairs spatial working memory performance. *The Journal of neuroscience : the official journal of the Society for Neuroscience* **17**, 8528-8535, doi:10.1523/JNEUROSCI.17-21-08528.1997 (1997).

84 Vijayraghavan, S., Wang, M., Birnbaum, S. G., Williams, G. V. & Arnsten, A. F. T. Inverted-U dopamine D1 receptor actions on prefrontal neurons engaged in working memory. *Nature Neuroscience* **10**, 376-384, doi:10.1038/nn1846 (2007).

85 Hu, G., Huang, X., Jiang, T. & Yu, S. Multi-Scale Expressions of One Optimal State Regulated by Dopamine in the Prefrontal Cortex. *Frontiers in physiology* **10**, 113-113, doi:10.3389/fphys.2019.00113 (2019).

86 Reinhart, R. M. G. & Nguyen, J. A. Working memory revived in older adults by synchronizing rhythmic brain circuits. *Nature Neuroscience* **22**, 820-827, doi:10.1038/s41593-019-0371-x (2019).

87 Chialvo, D. R., Cannas, S. A., Grigera, T. S., Martin, D. A. & Plenz, D. Controlling a complex system near its critical point via temporal correlations. *Scientific Reports* **10**, 12145, doi:10.1038/s41598-020-69154-0 (2020).

88 Xia, M., Wang, J. & He, Y. BrainNet Viewer: A Network Visualization Tool for Human Brain Connectomics. *PLOS ONE* **8**, e68910, doi:10.1371/journal.pone.0068910 (2013).

Competing interests

The authors declare no competing interests.

Contributions

L. Y. and J. F. conceived and designed the experiments. L.X. and L.Y. performed the experiments. L.X., L.Y., and J.F. wrote the paper. All authors revised the manuscript.

Data availability

All the codes supporting the findings of this study are available upon request to the authors.

Figure 1 Power-law distribution for the aggregate level reflecting the brain near criticality in the resting state. a Example of a point process (filled circles) extracted from one normalized ROI BOLD signal. **b** The probability distributions of group-aggregate avalanche sizes for the 1.4 SD thresholds and a time bin width of 1 volume (vol.) in the fMRI data. The distributions are well approximated by power laws with an exponent $\alpha = 1.56$ with Clauset's test $p = 0.99$, corresponding to $\kappa = 0.9912$ (histogram bins = 40) and branching parameter $\sigma = 0.9097$. Here, the lower bound x_{min} for MLE was set to 3. **c** The distribution of avalanche durations for the group-aggregated level can be fit well by a power law with an exponent $\tau = 1.84$ under the condition described in **b**, with Clauset's test $p = 0.33$. **d** There is a power-law relationship between the sizes and duration of the avalanches with a positive index $\gamma = 1.59$, which is close to $\frac{1-\tau}{1-\alpha} = 1.51$. **e** The branching ratio and power-law scaling exponents α of avalanche sizes for different thresholds used to define the point process.

Figure 2 Signatures of criticality as a function of MS in resting-state brain networks. a Top panel: The inverted-U trajectory of the MS $\langle r \rangle$ vs. SE $H(r)$. The line represents the significant quadratic fit of the data (F=615.835, p<0.001, R^2=0.808). Bottom panel: The frequency count for the distribution of MS $\langle r \rangle$. **b** The branching parameters σ vs. $\langle r \rangle$ for each subject. The green dashed line indicates $\sigma = 1$. The Pearson correlation value R and the p value are shown in the figure. The solid line is the linear regression. **c** Avalanche size distributions for the LMS group ($\langle r \rangle = 0.2824 \pm 0.0219$), MMS group ($\langle r \rangle = 0.5041 \pm 0.0042$) and HMS group ($\langle r \rangle = 0.6304 \pm 0.0246$). To demonstrate the difference among groups, we used gray lines with $\alpha = 1.47$ to guide the eyes. The corresponding group-aggregate branching parameters are $\sigma_{LS} = 0.7237$ for the LMS group, $\sigma_{MS} = 1.0123$ for the MMS group, and $\sigma_{MS} = 1.2023$ for the HMS group. **d** Avalanche duration distributions for three groups in **c**. To demonstrate the difference among groups, we used gray lines with $\tau = 1.7$ to guide the eyes. **e** Scaling relationship for the three groups. The blue line and purple line correspond to γ and $\frac{\tau-1}{\alpha-1}$, respectively. In the inset, $\delta = \left|\gamma - \frac{\tau-1}{\alpha-1}\right|$ indicates the distance to the critical point. **f** Quantification of brain state against three levels of $\langle r \rangle$ using kappa κ, which was calculated in different numbers of histogram bins.

Figure 3 Dependence of complexity in the FC network on the MS of BOLD signals. a Mean FC $\langle FC \rangle$ (averaged absolute values of elements from the FC matrix) as a function of MS $\langle r \rangle$. Dashed red line: linear fitting. The Pearson correlation value R and the p value shown in the figure are those calculated without outliers. **b** FC entropy $H(FC)$ as a function of MS $\langle r \rangle$. Dashed red line: quadratic fitting ($F = 2287.892$, p<0.001, $R^2 = 0.940$). **c** FC diversity $D(FC)$ as a function of MS $\langle r \rangle$. Dashed red line: quadratic fitting ($F = 1226.057$, p<0.001, $R^2 = 0.894$). **d** FC

flexibility CNE as a function of MS $\langle r \rangle$. Dashed red line: quadratic fitting ($F = 366.851$, $p<0.001$, $R^2 = 0.717$). The red circles represent participants with outliers that were not included in the linear fitting in **a** or quadratic fittings in **b**, **c**, and **d**.

Figure 4 The dependence of structure-function coupling on the MS of brain network. **a** Pearson correlation between anatomical and functional networks as a function of MS $\langle r \rangle$. The link density in the FC network $\rho_{FC} = 0.7$ and threshold in the SC network THR_{SC}=40 (corresponding to $\rho_{SC} = 0.4836$) are shown in the figure. Dashed red line: quadratic fitting ($F = 36.997$, $p<0.001$, $R^2 = 0.202$), which is better than linear fitting ($F = 39.346$, $p<0.001$, $R^2 = 0.118$). **b** Hamming distance $HD(FC - SC)$ between anatomical and FC as a function of MS $\langle r \rangle$. Dashed red line: quadratic fitting (F=36.997, $p<0.001$, R^2=0.202), which is better than linear fitting ($F = 39.346$, $p<0.001$, $R^2 = 0.118$). **c** The Pearson correlation between anatomical and functional connectivity networks as a function of FC density ρ_{FC} ($THR_{SC} = 40$ corresponding to $\rho_{SC} = 0.4826$) for the HMS, MMS, and LMS groups. **d** The Hamming distance between anatomical and functional connectivity networks as a function of FC density ρ_{FC} ($THR_{SC} = 40$ corresponding to $\rho_{SC} = 0.4826$) for the HMS, MMS, and LMS groups. In both **c** and **d**, green stars indicate significant differences between the HMS and MMS groups (two-sample t-test, p<0.05, uncorrected); purple stars indicate significant differences between the LMS and MMS groups (two-sample t-test, p<0.05, uncorrected).

Figure 5 The dynamic phase transition in individual subjects' brains. **a** The dependence of dynamic SE $\mathrm{H}(r)_n$ on dynamic MS $\langle r \rangle_n$ from six subjects selected randomly from the LMS, MMS, and HMS groups. The enlarged dark markers indicate the mean position for corresponding subjects (markers with the same shape). **b** The time-dependent changes in the Kuramoto order parameter $r(t)$ for six subjects as demonstrated in **a** (with the same color). **c** The normalized frequency count of $r(t)$ for different levels of $\langle r \rangle$, indicated by lines with different colors. **d** The dwell time (the time interval between two successive critical point crossing events) distribution for different levels of $\langle r \rangle$. **e** and **f** The distribution of vertical and horizontal moving distances of phase points in one step of the sliding window. **g** and **h** The vertical and horizontal velocities of state points of each subject as a function of their MS $\langle \mathrm{r} \rangle$. The vertical and horizontal velocities were calculated by $\frac{\langle |\Delta \langle r \rangle_n| \rangle}{\Delta n}$ and $\frac{\langle |\Delta \langle r \rangle_n| \rangle}{\Delta n}$, where the symbol $|\cdot|$ indicates the absolute value, and $\langle \cdot \rangle$ was the average across all the windows. Δn is the step used to slide the windows. Here, Δn =10 time points (volumes). Red dashed lines in **g** and **h**: quadratic fitting ($F = 139.316$, $p < 0.001$, $R^2 = 0.488$ in **g**; $F = 82.692$, $p < 0.001$, $R^2 = 0.362$ in **h**). Both quadratic fittings were better than linear fitting ($R^2 = 0.409$ in **g** and $R^2 = 0.275$ in **h**).

Figure 6 Dynamic modulations of FC complexity and structure-function coupling during the phase transition of brains. **a** The dependence of dynamic FC entropy as

a function of instantaneous MS; thick dashed white line: quadratic fitting (F=106350.82, p<0.001, R^2=0.877). **b** The dependence of dynamic FC diversity as a function of instantaneous MS. Thick dashed white line: quadratic fitting (F=80261.492 , p<0.001 , R^2=0.843). **c** The dependence of dynamic FC-SC correlation as a function of instantaneous MS; thick dashed white line: quadratic fitting (F=5519.072 , p<0.001 , R^2=0.270), which is better than linear fitting (R^2=0.225). **d** The dependence of dynamic FC-SC Hamming distance as a function of instantaneous MS; thick dashed white line: quadratic fitting (F=5519.072, p<0.001, R^2=0.270), which is better than linear fitting (R^2=0.225). In **a-d**, each dot represents a calculation from one window. The dots with the same color represent the calculation for one subject. However, due to the limited number of colors used, different subjects may share the same color. In **c-d**, a link density of 0.7 was used to threshold the FC network, and a threshold of 40 was used to threshold the structural network.

Figure 7 Correlations between cognitive performance scores and SE, as well as MS. **a-c** Correlation between SE and PMAT scores, picture vocabulary test scores, as well as the list sorting working memory test scores. Dashed red lines in **a-c**: linear fitting. **d** Scatterplot of the PMAT scores against the MS. The red dashed line represents the significant quadratic fit of the data (F=3.109, p=0.046, R^2=0.021), which is better than the linear fitting (R^2=0.007). **e** Scatterplot of the picture vocabulary test scores against the MS. Both the linear and quadratic regressions are not significant (linear: $p = 0.983$; quadratic: $p = 0.971$). **f** Scatterplot of the list sorting working memory test scores against the MS. The red dashed line represents the significant quadratic fit of the data (F=4.401, p=0.013, R^2=0.029), which is better than linear fitting (R^2=0.017).

Figure 8 The brain map for correlations between regional SE and PMAT. The color bar indicated the Pearson correlation value. The cortical and subcortical regions were defined by the Human Brainnetome Atlas (http://atlas.brainnetome.org/bnatlas.html). Data was visualized using BrainNet Viewer[88].

Table 1 The brain regions exhibited significant correlation between SE and PMAT.

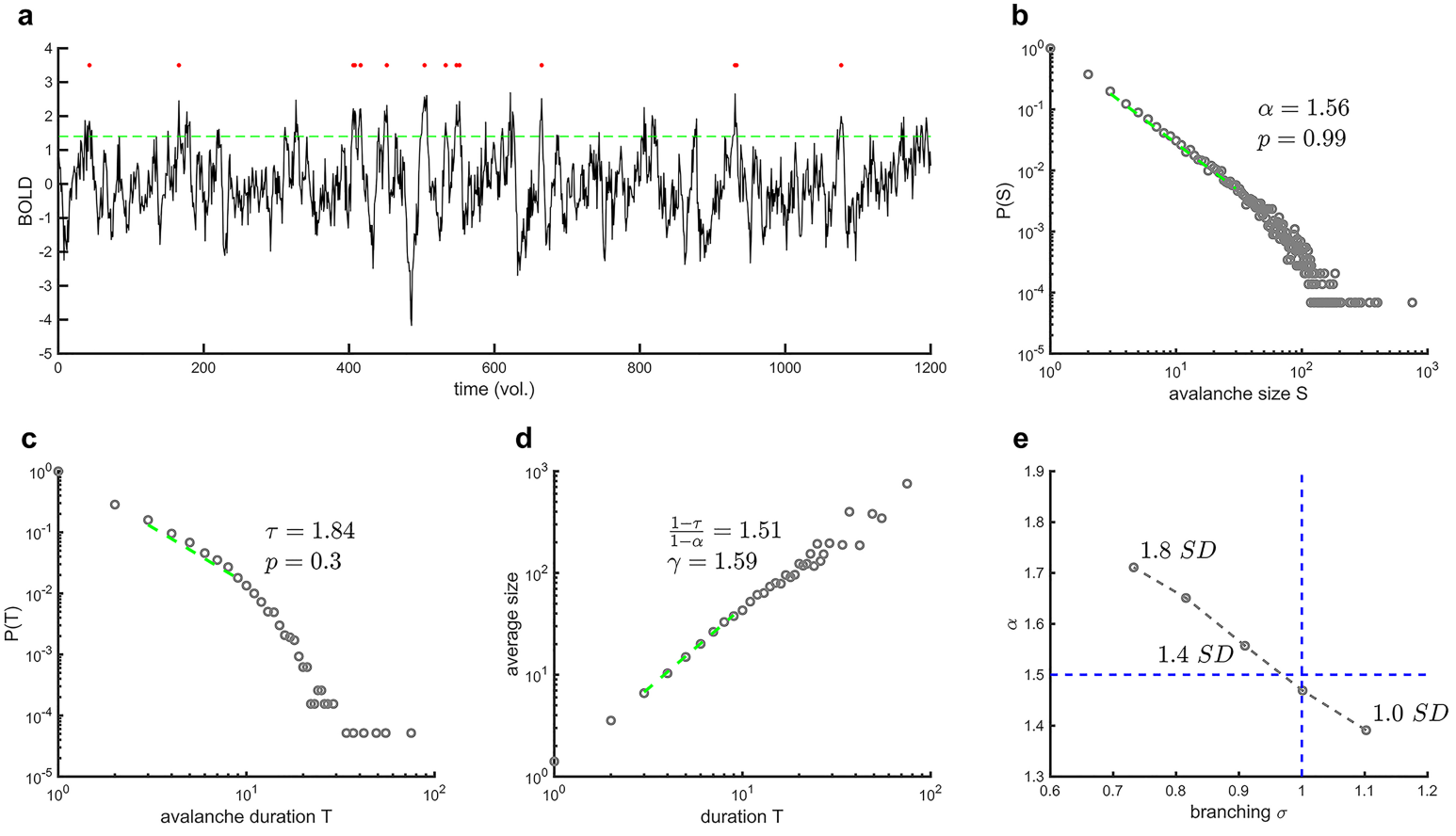
a
BOLD
time (vol.)
b
P(S)
avalanche size S
$\alpha = 1.56$
$p = 0.99$
c
P(T)
avalanche duration T
$\tau = 1.84$
$p = 0.3$
d
average size
duration T
$\frac{1-\tau}{1-\alpha} = 1.51$
$\gamma = 1.59$
e
α
branching σ
1.8 SD
1.4 SD
1.0 SD

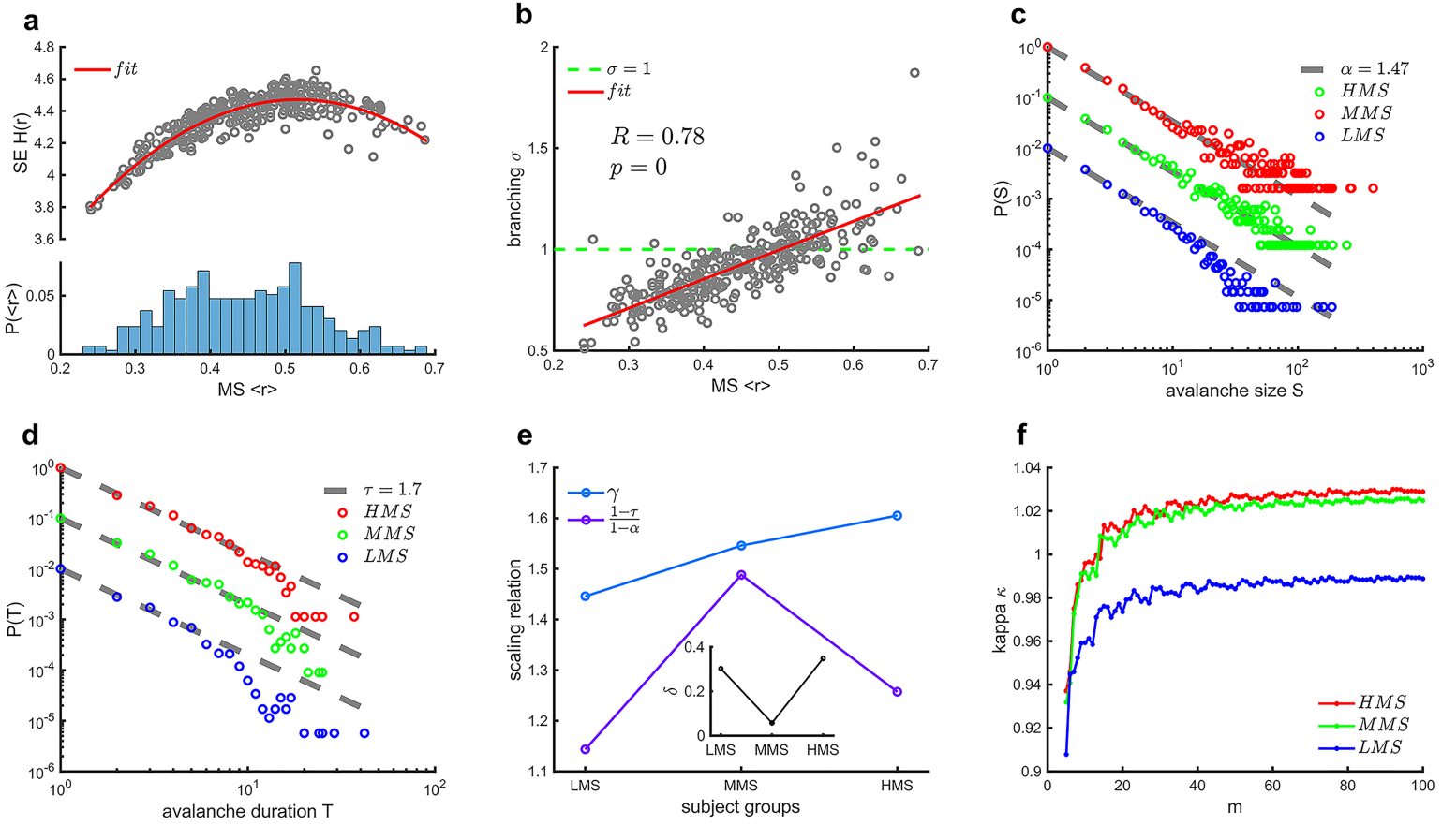
a
fit
SE H(r)
P(<r>)
MS <r>
b
σ = 1
fit
R = 0.78
p = 0
branching σ
MS <r>
c
α = 1.47
HMS
MMS
LMS
P(S)
avalanche size S
d
τ = 1.7
HMS
MMS
LMS
P(T)
avalanche duration T
e
γ
(1−τ)/(1−α)
scaling relation
δ
LMS
MMS
HMS
subject groups
f
kappa κ
HMS
MMS
LMS
m

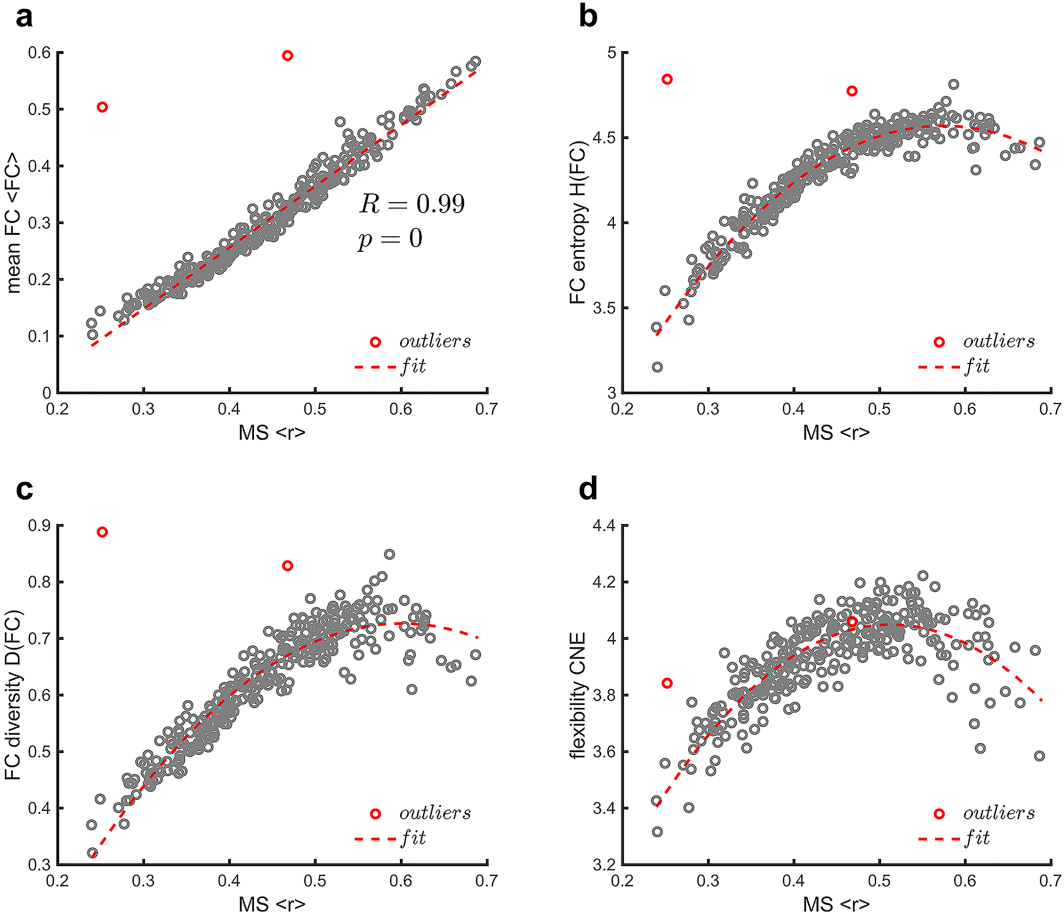
a
mean FC <FC>
MS <r>
$R = 0.99$
$p = 0$
outliers
fit
b
FC entropy H(FC)
MS <r>
outliers
fit
c
FC diversity D(FC)
MS <r>
outliers
fit
d
flexibility CNE
MS <r>
outliers
fit

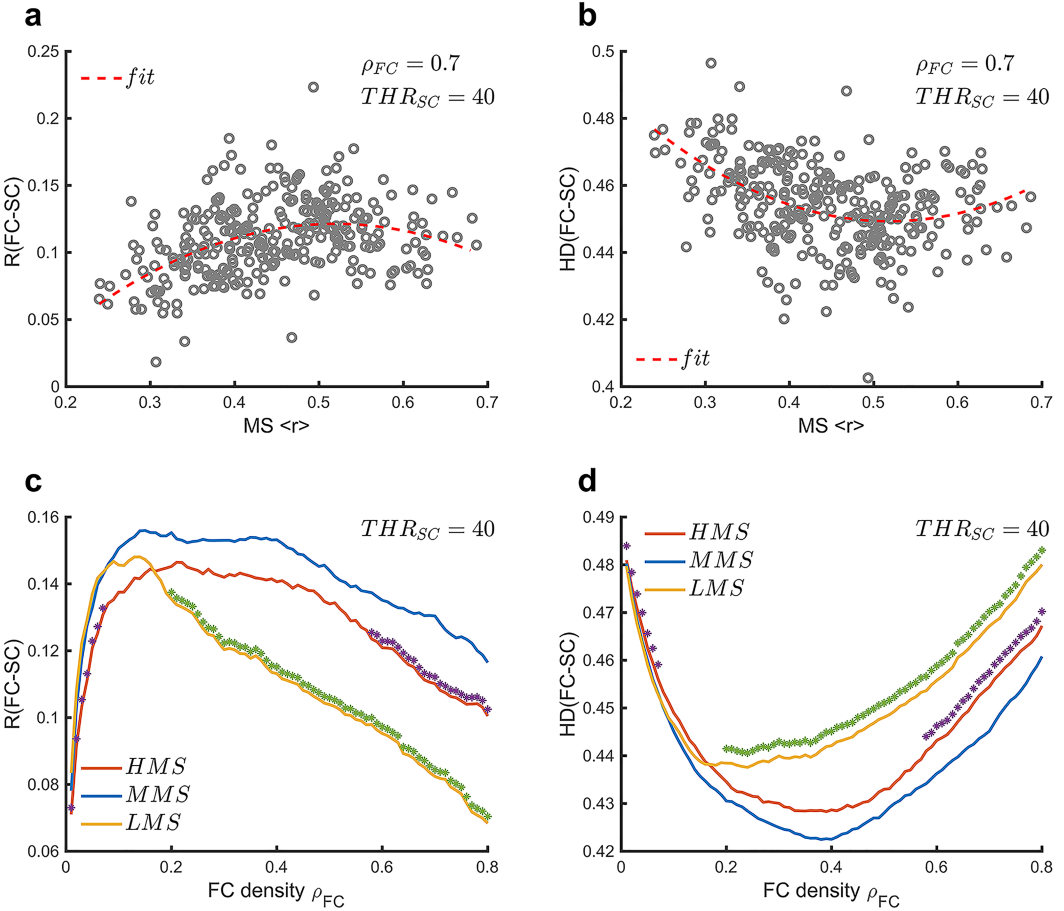
a
fit
$\rho_{FC} = 0.7$
$THR_{SC} = 40$
R(FC-SC)
MS <r>
b
$\rho_{FC} = 0.7$
$THR_{SC} = 40$
fit
HD(FC-SC)
MS <r>
c
$THR_{SC} = 40$
HMS
MMS
LMS
R(FC-SC)
FC density ρ_{FC}
d
$THR_{SC} = 40$
HMS
MMS
LMS
HD(FC-SC)
FC density ρ_{FC}

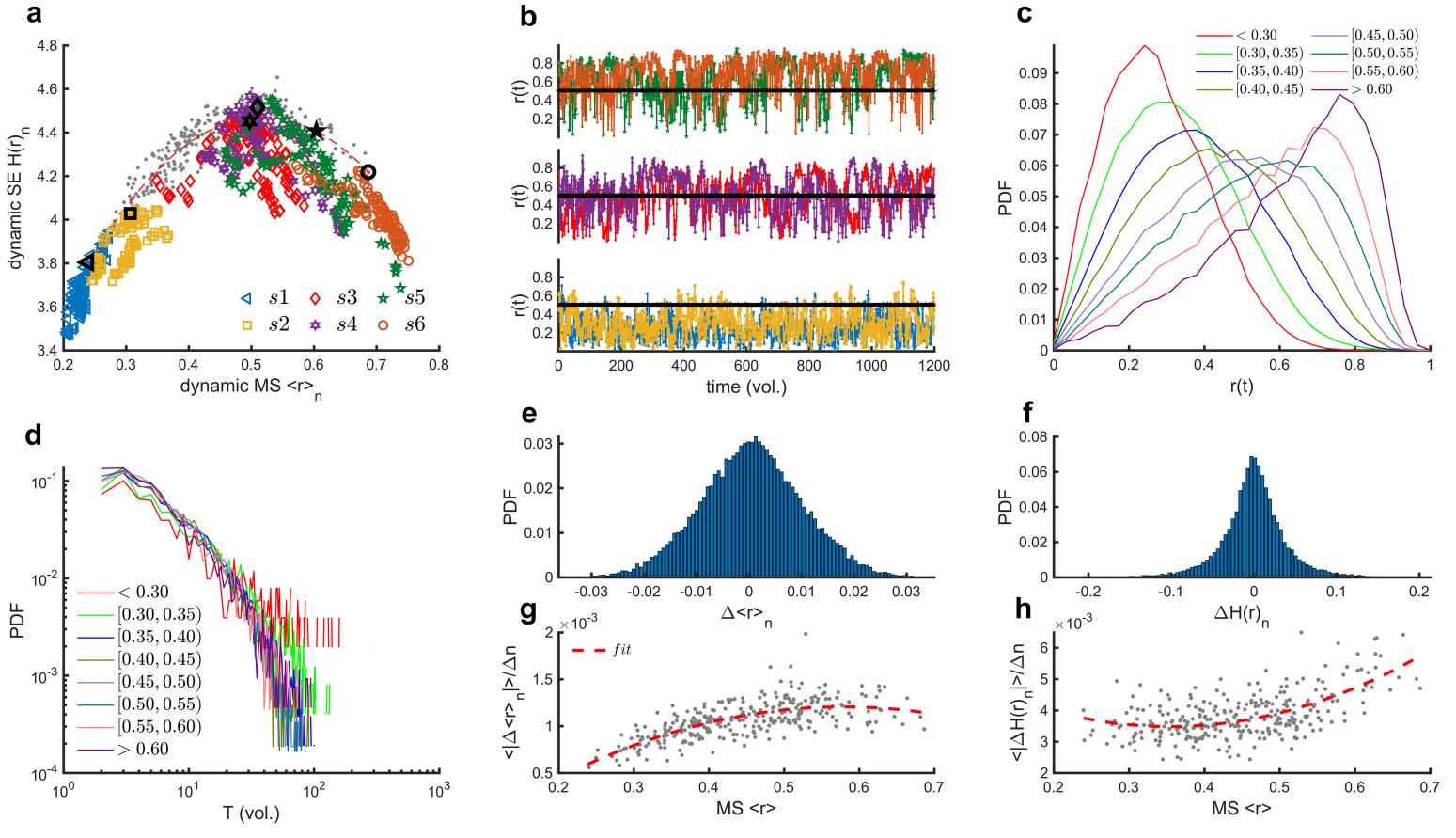
a
dynamic SE H(r)n
dynamic MS <r>n
s1
s2
s3
s4
s5
s6
b
r(t)
time (vol.)
c
< 0.30
[0.30, 0.35)
[0.35, 0.40)
[0.40, 0.45)
[0.45, 0.50)
[0.50, 0.55)
[0.55, 0.60)
> 0.60
PDF
r(t)
d
PDF
T (vol.)
e
PDF
Δ<r>n
f
PDF
ΔH(r)n
g
fit
<|Δ<r>n|>/Δn
MS <r>
h
<|ΔH(r)n|>/Δn
MS <r>

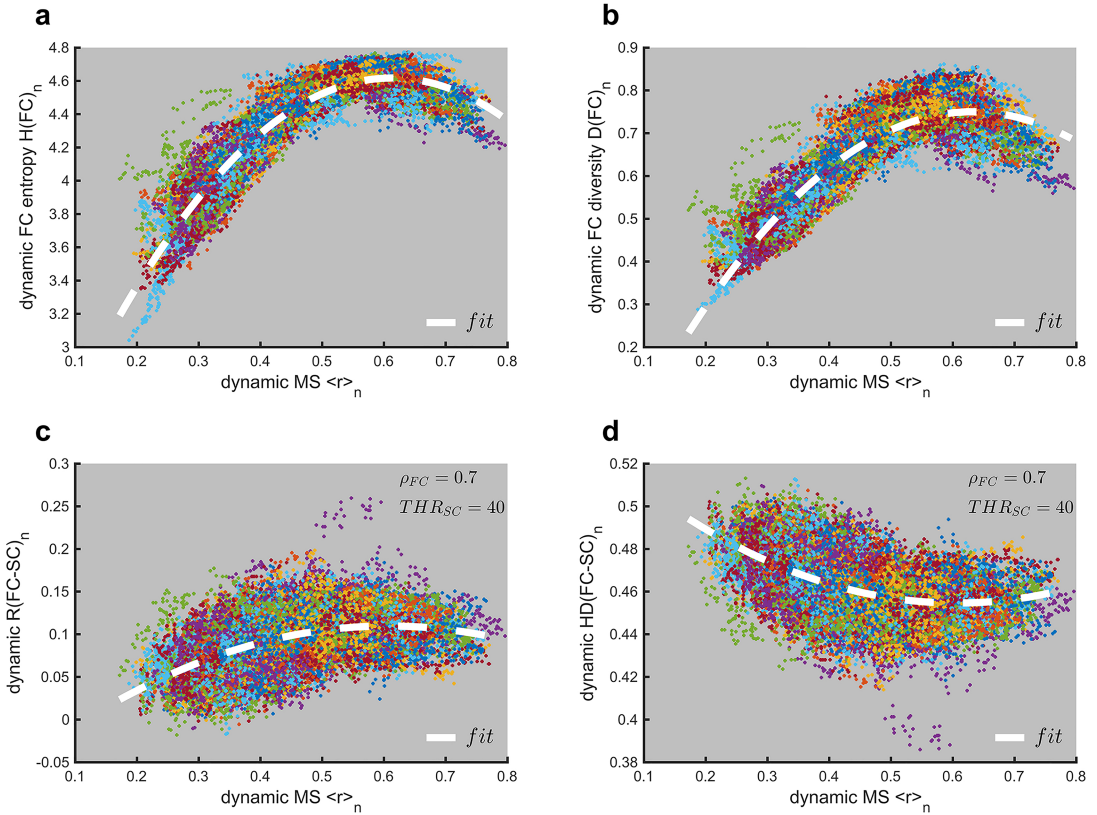
a
dynamic FC entropy H(FC)n
dynamic MS <r>n
fit
b
dynamic FC diversity D(FC)n
dynamic MS <r>n
fit
c
dynamic R(FC-SC)n
dynamic MS <r>n
ρFC = 0.7
THRSC = 40
fit
d
dynamic HD(FC-SC)n
dynamic MS <r>n
ρFC = 0.7
THRSC = 40
fit

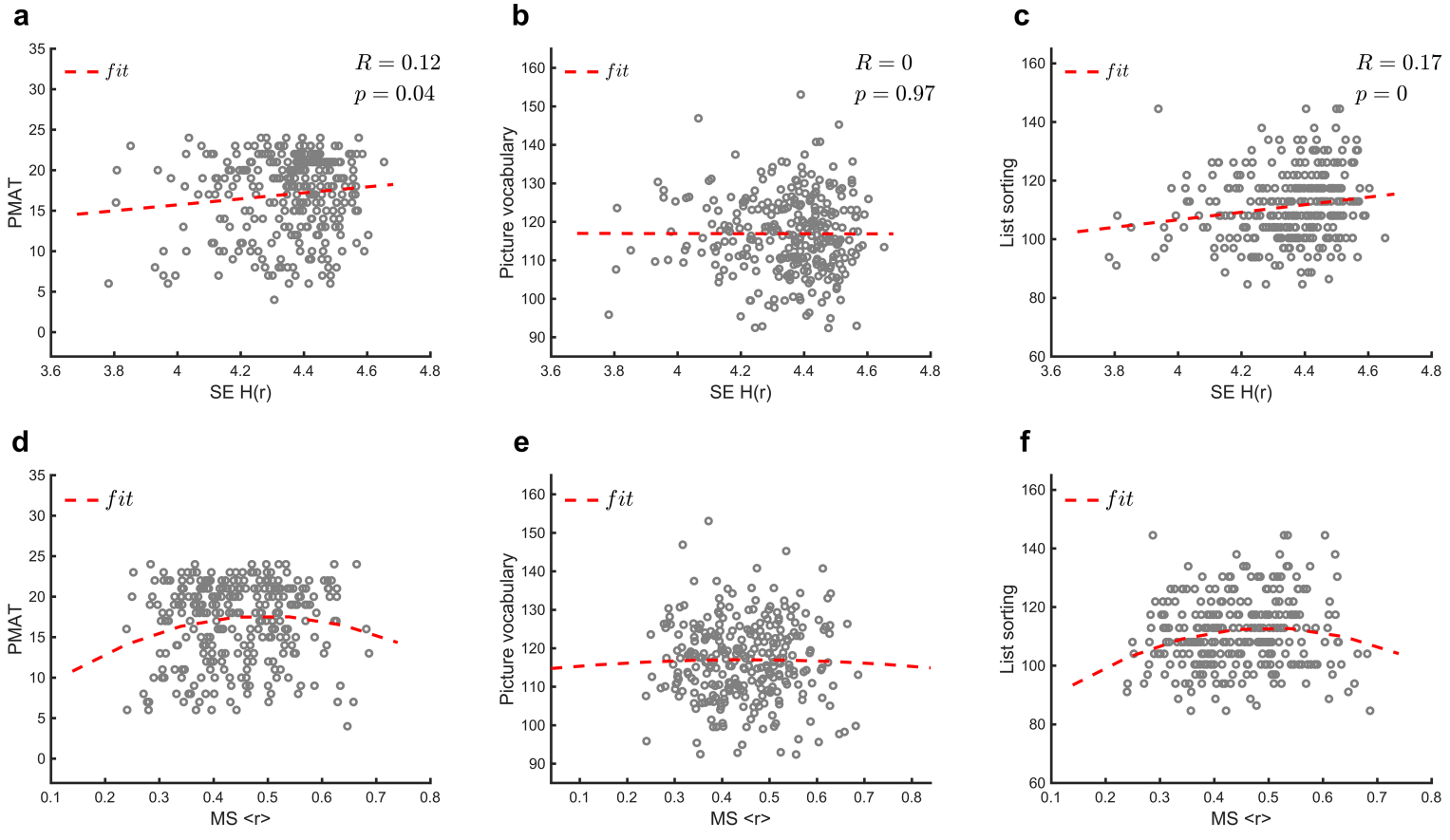
a
b
c
d
e
f
fit
R = 0.12
p = 0.04
R = 0
p = 0.97
R = 0.17
p = 0
PMAT
Picture vocabulary
List sorting
SE H(r)
MS <r>

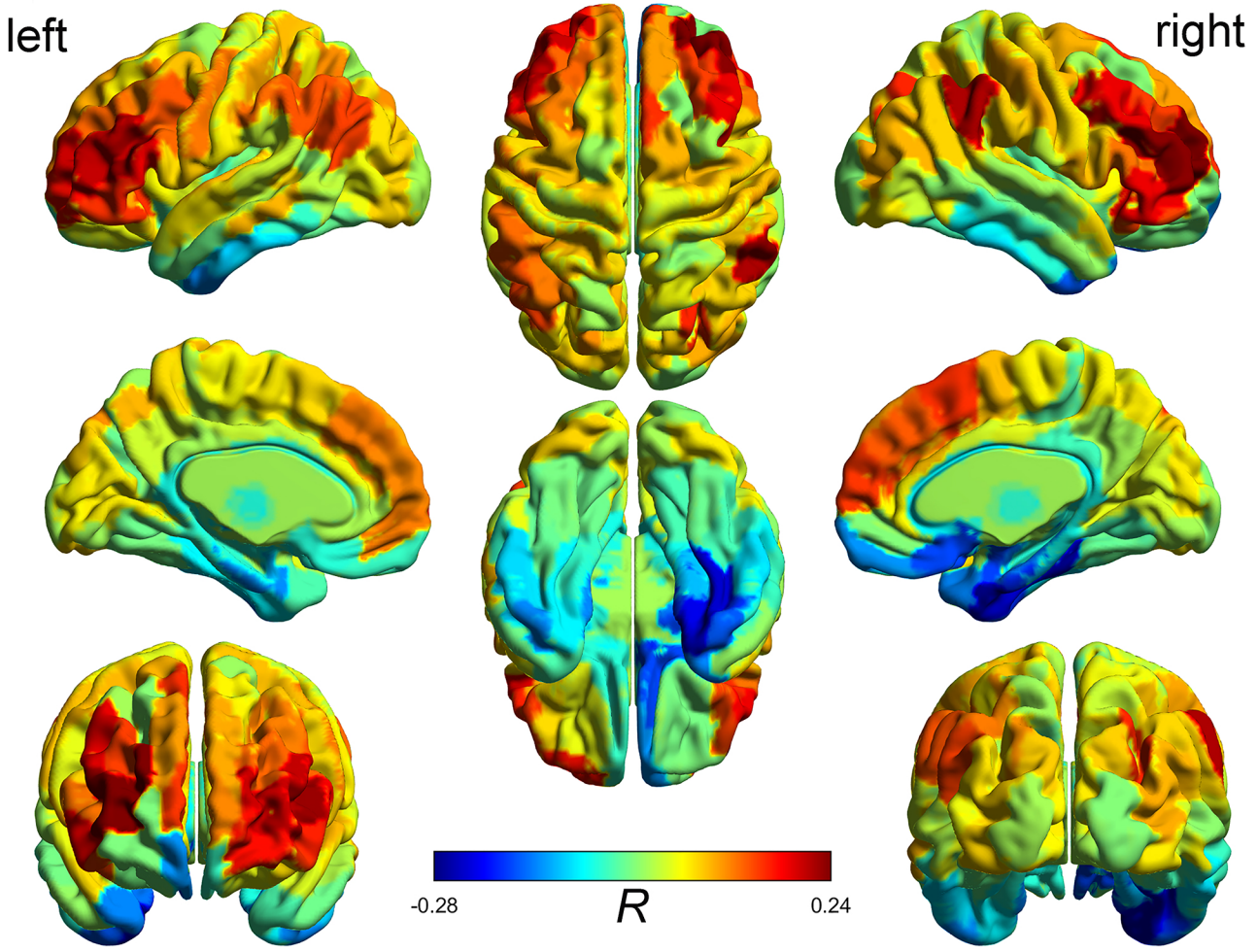
left
right
-0.28
R
0.24

Lobe	Gyrus	Left and right hemispheres	Modified cyto-architectonic	R value	P value (FDR corrected)
Frontal Lobe	MFG	MFG_R_7_2	inferior frontal junction	0.1744	0.0350
		MFG_L_7_3	area 46	0.2018	0.0131
		MFG_R_7_3	area 46	0.2425	0.0030
		MFG_L_7_4	ventral area 9/46	0.2047	0.0131
		MFG_R_7_4	ventral area 9/46	0.2340	0.0034
		MFG_R_7_5	ventrolateral area 8	0.1848	0.0268
		MFG_L_7_7	lateral area10	0.1683	0.0445
	IFG	IFG_L_6_2	inferior frontal sulcus	0.2269	0.0043
		IFG_L_6_3	caudal area 45	0.1784	0.0291
		IFG_R_6_4	rostral area 45	0.1837	0.0268
	OrG	OrG_R_6_6	lateral area 12/47	0.1853	0.0268
Parietal Lobe	IPG (Supramarginal Gyrus)	IPL_R_6_4	caudal area 40(PFm)	0.2166	0.0069

Abbreviations: MFG, Middle Frontal Gyrus; IFG, Inferior Frontal Gyrus; OrG, Orbital Gyrus; IPL, Inferior Parietal Lobule.